JM PAPERS

A momentum-conserving wake superposition method for wind-farm flows under pressure gradient

Bowen Du[1]**, Mingwei Ge**[1,†]**, Xintao Li**[1] **and Yongqian Liu**[1]

[1]State Key Laboratory of Alternate Electrical Power System with Renewable Energy Sources, North China Electric Power University, Beijing 102206, PR China

Pressure gradient over topography will significantly affect wind-farm flow. However, knowledge gaps still exist on how to superpose wind-turbine wakes in the wind-farm flow analytical model to account for this effect, leading to systematic errors in evaluating wind-farm wake effects. To this end, we derive an implicit momentum-conserving wake superposition method under pressure gradient (PG-IMCM) based on the total momentum deficit equation, which is linearised by the convection velocity introduced by Zong & Porté-Agel (*J. Fluid Mech.*, vol. 889, 2020, A8). The PG-IMCM method consists of the linear-weighted sum of individual velocity deficits, the sum of the individual pressure correction terms and the total pressure correction term. Based on a sensitivity analysis, we demonstrate that the last two terms nearly cancel out and, thus, can be neglected, resulting in a simplified form, which has the same form as its counterpart under zero pressure gradient but with the single-wake quantities redefined based on the wake model under pressure gradient. This motivates us to further examine the performance of the combination of five empirical superposition methods and the stand-alone wake model under pressure gradient. Validation results based on large-eddy simulation show that PG-IMCM has an overall satisfactory performance in both the magnitude and shape of the velocity-deficit profiles, provided that the stand-alone turbine wake can be modelled accurately, which is virtually identical with its simplified form. Further comparison with empirical superposition methods shows that local linear and wind product superposition methods based on the updated base flow also have comparable performance, with only discernable differences with the PG-IMCM method in the near-wake region of downstream turbines. Therefore, they are two attractive methods for engineering applications.

Key words: wakes

---

† Email address for correspondence: gemingwei@ncepu.edu.cn

1. Introduction

Accelerating wind energy deployment plays a vital role in the long-term reduction of greenhouse gas emissions. With the increasing scale and number of wind farms, flat terrain can no longer meet the construction needs of wind farms, and there is a high chance that they will be located on a non-flat complex terrain (Van Kuik *et al.* 2016). Compared with flat terrain, complex terrain will cause significant changes in the flow characteristics of the atmospheric boundary layer (Finnigan *et al.* 2020). As stated by Porté-Agel, Bastankhah & Shamsoddin (2020), there are three key aspects of the flow over topography that potentially influence the evolution of wind-turbine wakes: namely, (i) non-zero pressure gradients, (ii) terrain-induced streamline distortion and (iii) flow separation. These complex flow patterns pose a significant challenge to the performance of wind-farm flow analytical models (WFFAMs) and significantly limit numerous engineering applications such as wind farm designs and micro-site selections over complex terrain.

To deal with these problems, many researchers have carried out related studies based on large-eddy simulation (LES), and the results show that streamline distortion and flow separation mainly affect the elevation of the wake-centre trajectory from the ground (e.g. Shamsoddin & Porté-Agel 2018*b*; Liu, Lu & Ishihara 2021; Zhang *et al.* 2022*b*; Wang *et al.* 2023). Based on this physical insight, many WFFAMs are proposed to account for the baseflow streamline distortion induced by complex terrain. For instance, Feng, Shen & Li (2018) assumed that the centreline of wind-turbine wakes is parallel to the topography, and their wake velocity deficit can be evaluated using the Jensen model. In addition, the sum of squares superposition method is used to calculate the velocity in the merged wake region. Finally, they proposed a WFFAM and applied it to wind farm layout optimisation in a realistic complex terrain. Unlike Feng *et al.* (2018), Brogna *et al.* (2020) assumed that the wake centreline coincides with the background streamline passing through the rotor centre, and the wake velocity deficit can be calculated using the Gaussian wake model. Recently, Farrell *et al.* (2021) proposed a method that considers the heterogeneous background flow induced by complex terrain or mesoscale weather systems. Based on the Gaussian wake model, this method calculates the wake velocity deficit by dynamic coordinate transformation according to the baseflow streamline. Although this method has different computation details from Brogna *et al.* (2020), its essence is still to assume that the wake centre evolves downstream along the streamline. It should be noted that this method has been integrated into the open-source software package FLORIS developed by NREL (Farrell *et al.* 2021).

However, none of the above-mentioned WFFAMs takes into account the influence of pressure gradient on wake evolution. The seminal work of Shamsoddin & Porté-Agel (2018*a*) shows that pressure gradient will significantly affect the wind turbine wake recovery and wake width. Under favourable pressure gradient (FPG), wind-turbine wakes will recover faster, whereas their recovery will slow down under adverse pressure gradient (APG). Therefore, pressure gradient is one of the most important but frequently ignored factors affecting the performance of WFFAMs over complex terrain, and there is an urgent need to develop WFFAMs under pressure gradient. In general, a complete WFFAM under pressure gradient should consist of two parts: the wake model and the wake superposition method (Porté-Agel *et al.* 2020). A large body of literature exists which focuses on these two parts individually, and they are introduced in the following.

1.1. *Wake models under non-zero pressure gradient*

Wake models describe the spatial distribution of wake velocity deficit downstream of the stand-alone wind turbine. The majority of wake models do not consider the influence

999 A27-2

of pressure gradient, so they are only applicable to flat terrain conditions and cannot be applied directly to WFFAMs under pressure gradient. As a result, this subsection focuses only on the wake models under pressure gradient. Readers interested in the zero-pressure-gradient (ZPG) wake models are referred to the related reviews (Crespo, Hernandez & Frandsen 1999; Stevens & Meneveau 2017; Archer *et al.* 2018, among others).

Based on the experimental observation that the ratio λ of the maximum velocity deficit C to the wake width σ is independent of the pressure gradient (Thomas & Liu 2004), Shamsoddin & Porté-Agel (2017, 2018*a*) derived analytical wake models for the turbulent planar and axisymmetric wakes under pressure gradient for the first time. The derivation of the models takes advantage of the Bernoulli relation to replace the pressure gradient with the background velocity in the *x*-momentum equation. Moreover, it assumes the wake velocity deficit has a self-similar axisymmetric Gaussian distribution. Finally, a nonlinear ordinary differential equation (ODE) and an asymptotic solution for C at each *x*-position are proposed based on the integral form of the *x*-momentum equation. Compared with the experimental and LES results, it is shown that the proposed models can accurately predict the influence of arbitrary pressure gradient on the evolution of the turbulent planar and axisymmetric wakes. Since turbulent axisymmetric wakes can be viewed as a simplification of wind-turbine wakes, the analytical model also applies to wind-turbine wakes (Shamsoddin & Porté-Agel 2018*b*; Dar & Porté-Agel 2022).

Based on this model, Dar & Porté-Agel (2022) further considered the pressure gradient induced by the wind rotor and proposed a new method to determine the initial value of velocity deficit in the near-wake region based on the Bernoulli equation, improving the performance of the model in escarpment cases. Recently, Dar, Gertler & Porté-Agel (2023) systematically studied the effects of pressure gradients on some important wake characteristics, such as near-wake length and wake growth rate, using wind tunnel experiments on constant slope ramps with different inclination angles. It is shown that the analytical model designed for wakes under pressure gradient can improve the wake deficit prediction significantly when the ZPG wake model fails.

1.2. *Wake superposition methods under ZPG*

When a specific location in the wind farm is affected by the wakes of more than one wind turbine, the wake velocity deficit at that location needs to be determined by wake superposition methods. The wake superposition method is an essential factor affecting the performance of WFFAMs, and existing wake superposition methods are all proposed for the ZPG condition (Porté-Agel *et al.* 2020). Early wake superposition models are all empirical expressions without solid theoretical foundations. Lissaman (1979) assumed that the distance between wind turbines in a wind farm is large, and thus the wake interference is minimal. Therefore, the velocity deficit can be regarded as a passive scalar, and the cumulative wake velocity deficit generated by multiple wind turbines is similar to the pollutant concentration of multiple plumes. Based on this assumption, the merged wake velocity deficit can be obtained by linearly superposing the velocity deficits generated by different wind turbines. In contrast, Katic, Højstrup & Jensen (1986) assumed that the total kinetic energy deficit within the superposition region is equal to the accumulation of individual wake kinetic energy deficits, and they proposed the widely used sum of squares superposition principle. It is noteworthy that the two described superposition methods calculate the wake velocity deficit or kinetic energy deficit based on the freestream wind speed U_∞, which may lead to the overestimation of these two quantities of the waked turbine. To this end, Voutsinas, Rados & Zervos (1990) developed a new wake

superposition method based on the sum of squares superposition of the local kinetic energy deficits, which are defined by the local incoming flow speed u_0^i for the ith turbine. Similarly, Niayifar & Porté-Agel (2016) use u_0^i as the reference speed to calculate the local velocity deficits but linearly superimpose them to calculate wind-farm flows. According to the different definitions of the velocity deficit caused by the ith turbine and different superposition principles, the wind-farm flow velocity deficit U_s obtained by the four described superposition methods are denoted and written as follows:

$$\text{Global linear:} \quad U_s(x, y, z) = \sum_i (U_\infty - u_w^i(x, y, z)), \tag{1.1}$$

$$\text{Global square:} \quad U_s(x, y, z) = \sqrt{\sum_i (U_\infty - u_w^i(x, y, z))^2}, \tag{1.2}$$

$$\text{Local linear:} \quad U_s(x, y, z) = \sum_i (u_0^i - u_w^i(x, y, z)), \tag{1.3}$$

$$\text{Local square:} \quad U_s(x, y, z) = \sqrt{\sum_i (u_0^i - u_w^i(x, y, z))^2}. \tag{1.4}$$

Here, u_w^i represents the wake velocity of the ith wind turbine and can be calculated through the wake model.

Recently, Lanzilao & Meyers (2022) proposed a novel recursive relation capable of merging wind-turbine wakes, which can be called wind product:

$$\text{Wind product:} \quad U_s(x, y, z) = U_\infty - U_\infty \prod_i \left(\frac{u_w^i(x, y, z)}{u_0^i} \right). \tag{1.5}$$

By comparing its prediction with LES and supervisory control and data acquisition data, they found that the performance of this wake superposition method is very close to the local linear method, with a similar mean absolute error (MAE) in a homogeneous background velocity field, whereas it displays a lower MAE in the case of a heterogeneous background velocity, which may be applicable for the cases under pressure gradient. It is noteworthy that the wind product method has a different form from the other superposition methods. As shown in (1.1)–(1.4), the total wind-farm flow velocity deficit U_s is calculated as the sum of individual velocity deficits in a specific way. In contrast, the wind product method directly calculates the wind-farm flow U_w as a product of U_∞ with normalised individual wake velocity of each turbine. Finally, U_s is obtained by subtracting U_w from the base flow U_∞.

Although these superposition models claim to conserve momentum or energy deficit, they make many unreasonable assumptions, so they are all empirical methods that need to be improved. To this end, Zong & Porté-Agel (2020) proposed a superposition method that conserves the total momentum deficit in the streamwise direction for the first time. By defining the mean wake convection velocity $u_c^i(x)$ and $U_c(x)$ of the single-alone wind turbine wake and the combined wake, respectively, a linear weighted wake superposition method is proposed. The weight of the contribution of the ith wind turbine to the wind farm is $u_c^i(x)/U_c(x)$. The expression is as follows:

$$\text{IMCM:} \quad U_s(x, y, z) = \sum_i \frac{u_c^i(x)}{U_c(x)} (u_0^i - u_w^i(x, y, z)). \tag{1.6}$$

Since the determination of $U_c(x)$ relies on U_s and $U_\infty - U_s$, this method needs an iterative method (Zong & Porté-Agel 2020). Therefore, we denote it as the implicit momentum-conserving method (IMCM). Compared with wind tunnel measurements and LES results, this method outperforms all the empirical methods by accurately predicting the power production and the centreline wake velocity deficit (Zong & Porté-Agel 2020).

In addition, Bastankhah *et al.* (2021) developed a fairly simple explicit relationship that predicts the streamwise velocity distribution within a wind farm by solving an approximate form of conservation of mass and momentum for a turbine in a wind farm array (Bay *et al.* 2023; Blondel 2023). As this model is obtained by solving flow-governing equations directly for a turbine that is subject to upwind turbine wakes, no *ad hoc* superposition technique is needed to predict wind-farm flows. Therefore, this model essentially differs from the superposition methods introduced above, which rely on the stand-alone wake model. Here, we do not intend to account for the effect of pressure gradient by explicitly solving the integral Reynolds-averaged Navier–Stokes (RANS) equation, which is far beyond the scope of this study.

1.3. *The present work*

In summary, previous studies mainly focused on the wake model under pressure gradient and wake superposition methods under the ZPG condition. Until recently, Dar & Porté-Agel (2024) proposed to extend the application of the analytical wake model under pressure gradient to multiple turbine wakes by updating the effective background velocity for wind turbines from upstream to downstream. Although their method has only been validated in the aligned layout, it can be extended to arbitrary wind-farm layouts with minor modifications. From the perspective of wake superposition, their method is very similar to the wind product method proposed by Lanzilao & Meyers (2022) but accounts for the influence of pressure gradient on the single-wake evolution. Nevertheless, the research on the wake superposition method and WFFAM under pressure gradient is still at a very early stage, and there is much work that needs to be done. As demonstrated by Zong & Porté-Agel (2020) and Bastankhah *et al.* (2021), the momentum-conserving methods under the ZPG condition have superior performance compared with empirical superposition methods. Therefore, a momentum-conserving method under pressure gradient is the focus of this study, which has not been proposed previously. Specifically, we theoretically derive an implicit momentum-conserving wake superposition model under pressure gradient (PG-IMCM), show its simplified form and validate their performance against high-fidelity LES results. Moreover, five empirical WFFAMs under pressure gradient based on (1.1)–(1.5) are further developed and inter-compared.

The remainder of the article is as follows. The model development is elaborated on in § 2. In § 3, the LES methodology and validation cases set-up are introduced. The performance of the momentum-conserving method is validated in § 4. In § 5, we further extend the empirical superposition methods to account for pressure gradient and compare their performance against LES results. Finally, conclusions are given in § 6.

2. Model development

In this section, we show the proposed momentum-conserving WFFAM under pressure gradient with an emphasis on the derivation of the implicit momentum-conserving wake superposition model under pressure gradient (PG-IMCM) in § 2.1. The single turbine wake model under pressure gradient is given in § 2.2. Moreover, a simplified version of PG-IMCM is presented in § 2.3.
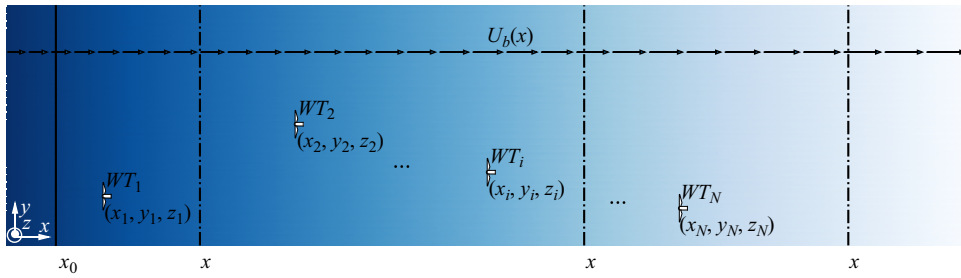
Figure 1. Schematic of a wind farm with an arbitrary layout consisting of *N* wind turbines under FPG. (Dark blue represents the high-pressure region, whereas light blue represents the low-pressure region.)

2.1. *Theoretical derivation of PG-IMCM*

2.1.1. *Total momentum deficit under pressure gradient*

Here, we consider a wind farm with N wind turbines $(WT_1, \ldots, WT_i, \ldots, WT_N)$ under pressure gradient with the base flow $U_b(x)$, as depicted in figure 1. The wind turbines are assumed to have the same rotor diameter D. The position of WT_i is labelled as (x_i, y_i, z_i), where x, y and z are the streamwise, spanwise and vertical coordinates, respectively. Wind turbines are ordered with respect to their streamwise positions to ensure $x_i \geq x_{i-1}$. The RANS streamwise momentum equation for wind-farm flows can be written as follows:

$$U_w \frac{\partial U_w}{\partial x} + V \frac{\partial U_w}{\partial y} + W \frac{\partial U_w}{\partial z} = -\frac{1}{\rho} \frac{\partial P}{\partial x} - \frac{\partial \overline{u'u'}}{\partial x} - \frac{\partial \overline{u'v'}}{\partial y} - \frac{\partial \overline{u'w'}}{\partial z} + \frac{f_t}{\rho}. \tag{2.1}$$

Here, U_w, V and W are the streamwise, spanwise and vertical velocity of the wind-farm flow, respectively, $\overline{u'u'}$, $\overline{u'v'}$ and $\overline{u'w'}$ are the Reynolds stress components, P is the time-averaged static pressure, ρ is the air density and f_t is the body force caused by wind turbines, which can be expressed as (Bastankhah *et al.* 2021):

$$\frac{f_t}{\rho} = \sum_{i=1}^{N} -\frac{T_i}{\rho \pi R^2} \delta(x - x_i) \mathcal{H}(R^2 - [(y - y_i)^2 + (z - z_i)^2]), \tag{2.2}$$

where T_i is the thrust of WT_i, R is the rotor radius, $\delta(x)$ is the Dirac delta function and $\mathcal{H}(x)$ is the Heaviside step function. The viscous term is neglected due to the high Reynolds number in the atmospheric boundary layer. It is noteworthy that we only consider the background pressure variations induced by complex terrain and neglect the sudden pressure changes in the near-wake region of the wind rotor (Dar & Porté-Agel 2022). Therefore, the streamwise pressure gradient $\partial P/\partial x$ and the streamwise variation of the background velocity $U_b(x)$ satisfy the Bernoulli equation under the considered conditions, i.e. $1/\rho \, \partial P/\partial x = -(\mathrm{d}U_b/\mathrm{d}x)U_b$. The governing equation for the wind-farm flow velocity deficit $U_s(x, y, z) = U_b(x) - U_w(x, y, z)$ can be derived by subtracting (2.1) from $U_w \partial U_b/\partial x$, with the assumption of $\partial U_b/\partial y = \partial U_b/\partial z = 0$:

$$U_w \frac{\partial U_s}{\partial x} + V \frac{\partial U_s}{\partial y} + W \frac{\partial U_s}{\partial z} = -\frac{\mathrm{d}U_b}{\mathrm{d}x} U_s + \frac{\partial \overline{u'u'}}{\partial x} + \frac{\partial \overline{u'v'}}{\partial y} + \frac{\partial \overline{u'w'}}{\partial z} - \frac{f_t}{\rho}. \tag{2.3}$$

In addition, considering the continuity equation,

$$\frac{\partial U_w}{\partial x} + \frac{\partial V}{\partial y} + \frac{\partial W}{\partial z} = 0, \tag{2.4}$$

we can obtain the following:

$$U_w \frac{\partial U_s}{\partial x} + V \frac{\partial U_s}{\partial y} + W \frac{\partial U_s}{\partial z} = \frac{\partial U_w U_s}{\partial x} + \frac{\partial V U_s}{\partial y} + \frac{\partial W U_s}{\partial z}. \tag{2.5}$$

Substituting (2.5) into (2.3) yields

$$\frac{\partial U_w U_s}{\partial x} + \frac{\partial V U_s}{\partial y} + \frac{\partial W U_s}{\partial z} = -\frac{\mathrm{d} U_b}{\mathrm{d} x} U_s + \frac{\partial \overline{u' u'}}{\partial x} + \frac{\partial \overline{u' v'}}{\partial y} + \frac{\partial \overline{u' w'}}{\partial z} - \frac{f_t}{\rho}. \tag{2.6}$$

Then, we can take the y–z plane integral from x_0 (a location upstream of the wind farm) to x (an arbitrary location within or downstream of the wind farm). The upper and lower bounds of the y- and z-integration are selected far from the wind farm to ensure U_s, $\overline{u' v'}$ and $\overline{u' w'}$ all vanish (in a given x-normal plane). Therefore, the integrals of the terms inclusive of the y- or z-derivative in (2.6) are zero. In addition, the integral of normal Reynolds stress component $\iint \overline{u' u'} \, \mathrm{d} y \, \mathrm{d} z |_{x_0}^x$ is negligible, compared with other terms according to the budget comparison of Bastankhah *et al.* (2021). Therefore, the final expression for the total momentum deficit under pressure gradient is

$$\iint U_w(x, y, z)[U_b(x) - U_w(x, y, z)] \, \mathrm{d} y \, \mathrm{d} z$$
$$= \sum_{i \in B} \frac{T_i}{\rho} - \iint \underbrace{\int_{x_0}^x \frac{\mathrm{d} U_b(x')}{\mathrm{d} x'} U_s(x', y, z) \, \mathrm{d} x'}_{\mathfrak{P}(x, y, z)} \, \mathrm{d} y \, \mathrm{d} z. \tag{2.7}$$

Here, $B = \{i \, | \, x_i < x\}$ and $\mathfrak{P}(x, y, z)$ is the pressure correction term induced by the wind-farm velocity deficit. The equation shows that the total momentum deficit for a wind farm under pressure gradient consists of two parts: the total thrust of wind turbines and the integral of $\mathfrak{P}(x, y, z)$, which is related to the pressure gradient.

2.1.2. *General expression for the wind-turbine thrust under pressure gradient*

To proceed with our derivation, we introduce some new velocity variables. To begin with, we give the rules of nomenclature as follows: u^i represents the velocity variables of WT_i, whereas U^i represents the velocity variables associated with i wind turbines; The subscripts s, w and b represent the velocity deficit, the wake velocity and the base flow, respectively. By definition, $U_b^i = U_b$. Subsequently, we choose two control volumes, including i and $i - 1$ wind turbines, whose upper bound of the streamwise coordinate is larger than x_i. The only difference is that the latter excludes WT_i, as depicted in figure 2. In this condition, if we apply (2.7) to these two control volumes and subtract one from the other, we can obtain the expression for the thrust of WT_i as follows:

$$\frac{T_i}{\rho} = \iint U_w^i(x, y, z)[U_b(x) - U_w^i(x, y, z)] \, \mathrm{d} y \, \mathrm{d} z$$
$$- \iint U_w^{i-1}(x, y, z)[U_b(x) - U_w^{i-1}(x, y, z)] \, \mathrm{d} y \, \mathrm{d} z$$
$$+ \iint \int_{x_i - \delta x}^x \frac{\mathrm{d} U_b(x')}{\mathrm{d} x'} [U_w^{i-1}(x', y, z) - U_w^i(x', y, z)] \, \mathrm{d} x' \, \mathrm{d} y \, \mathrm{d} z, \tag{2.8}$$
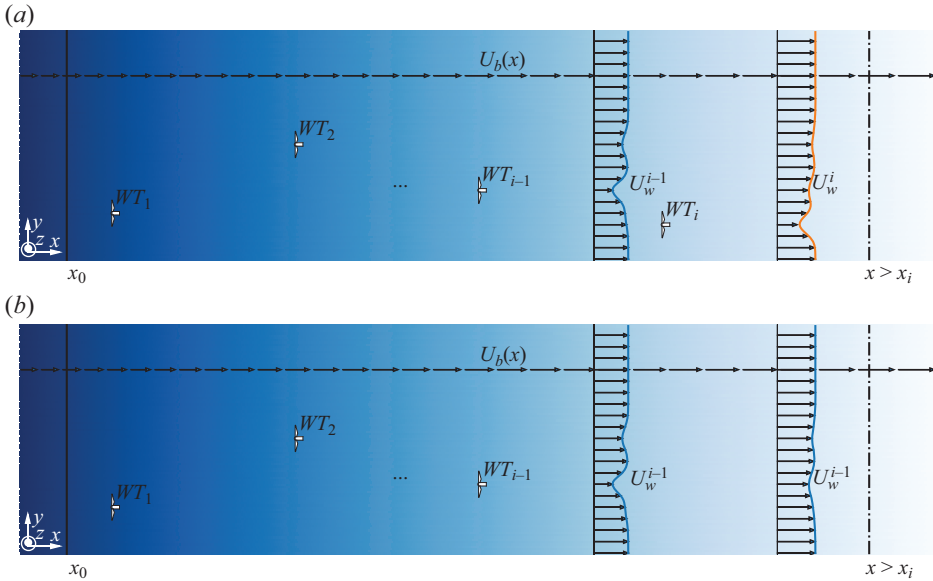
Figure 2. Schematic of the control volume for (*a*) *i* wind turbines and (*b*) *i* − 1 wind turbines under FPG. (*b*) is the same as (*a*) in the absence of WT_i.

where δ_x represents an infinitely small distance, U_w^i and U_w^{i-1} are the streamwise velocity of the wind-farm flow with i wind turbines and $i-1$ wind turbines, respectively. Here $U_w^{i-1} - U_w^i$ is essentially the wake velocity deficit u_s^i induced by WT_i, which can be modelled by the wake model under pressure gradient. As has been demonstrated by Bastankhah *et al.* (2021), the first and second terms on the right-hand side of (2.8) can be simplified as follows:

$$\iint U_w^i[U_b(x) - U_w^i]\, \mathrm{d}y\, \mathrm{d}z - \iint U_w^{i-1}[U_b(x) - U_w^{i-1}]\, \mathrm{d}y\, \mathrm{d}z$$

$$= \iint U_w^i(U_w^{i-1} - U_w^i)\, \mathrm{d}y\, \mathrm{d}z - \iint (U_w^{i-1} - U_w^i)[U_b(x) - U_w^{i-1}]\, \mathrm{d}y\, \mathrm{d}z$$

$$\leq \iint U_w^i(U_w^{i-1} - U_w^i)\, \mathrm{d}y\, \mathrm{d}z = \iint (U_w^{i-1} - u_s^i)u_s^i\, \mathrm{d}y\, \mathrm{d}z. \tag{2.9}$$

Generally speaking, $U_w^{i-1}(x, y, z)$ is a three-dimensional spatial-varying velocity distribution, which is influenced by the cumulative effect of $i-1$ wind-turbine wakes and is essentially the base flow for WT_i. To further simplify our derivation, we assume the use of $u_b^i(x)$ to replace U_w^{i-1}. It should be noted that $u_b^i(x)$ may differ significantly from $U_b(x)$ depending on the wind-farm layout, as it can be influenced by upstream wind-turbine wakes. As a result, the modified momentum deficit can be approximated as follows:

$$\iint (U_w^{i-1} - u_s^i)u_s^i\, \mathrm{d}y\, \mathrm{d}z \approx \iint [u_b^i(x) - u_s^i]u_s^i\, \mathrm{d}y\, \mathrm{d}z, \tag{2.10}$$

where $u_b^i(x) - u_s^i = u_w^i$ is the wake velocity of WT_i accounting for the base flow variation.

In our study, $u_b^i(x)$ is modelled as the average wind speed in the rotor area behind WT_i, which is sampled in U_w^{i-1} to represent different wake interference conditions, such
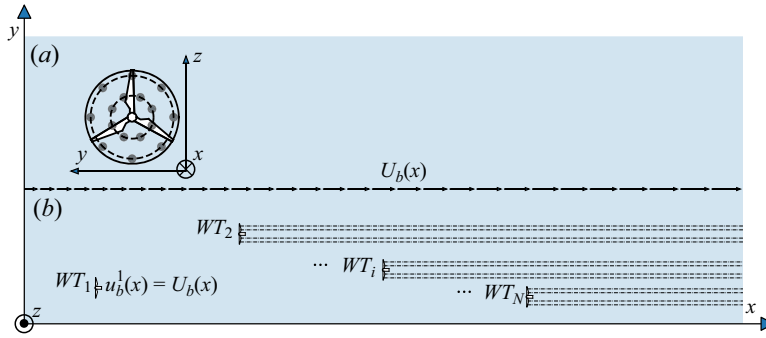
999 A27-8

Figure 3. Schematic of (*a*) quadrature points at the rotor plane of WT_i and (*b*) velocity sampling lines of WT_i ($i \geq 2$).

as full wake and partial wake. To save computational costs, we approximate $u_b^i(x)$ using the average of $N_q = 16$ velocity sampling lines downstream of WT_i, whose spanwise and vertical coordinates ($y_{i,q}$ and $z_{i,q}$) are the same as the quadrature points evenly divided over the rotor area of WT_i, as shown in figure 3. The coordinates of the quadrature points can be found in Allaerts & Meyers (2019), which is adopted to calculate the rotor equivalent wind speed. The expression for $u_b^i(x)$ is defined as follows:

$$u_b^i(x) = \frac{1}{N_q} \sum_{q=1}^{N_q} U_w^{i-1}(x, y_{i,q}, z_{i,q}) = U_b(x) - \frac{1}{N_q} \sum_{q=1}^{N_q} U_s^{i-1}(x, y_{i,q}, z_{i,q}). \qquad (2.11)$$

For $i = 1$, $u_b^1(x) = U_b(x)$, whereas for $i \geq 2$, $u_b^i(x)$ can be obtained through a recursive procedure, which is detailed in Appendix A. It should be noted that this modelling for $u_b^i(x)$ is different from Dar & Porté-Agel (2024), who use the wind speed in the wake centreline behind WT_i as $u_b^i(x)$, which may be only applicable for the aligned wind farm layout. In contrast, our proposed modelling for $u_b^i(x)$ can be applicable for arbitrary wind farm layouts.

Finally, the thrust of WT_i can be expressed as

$$\frac{T_i}{\rho} = \iint u_w^i(x, y, z)[u_b^i(x) - u_w^i(x, y, z)] \, \mathrm{d}y \, \mathrm{d}z$$
$$+ \iint \underbrace{\int_{x_i-\delta x}^{x} \frac{\mathrm{d}U_b(x')}{\mathrm{d}x'} u_s^i(x', y, z) \, \mathrm{d}x'}_{\mathfrak{p}^i(x,y,z)} \, \mathrm{d}y \, \mathrm{d}z. \qquad (2.12)$$

Here, $\mathfrak{p}^i(x, y, z)$ is the pressure correction term induced by individual velocity deficit.

2.1.3. *Linearised expression for the wind-turbine thrust under pressure gradient*
It has been shown that the wake velocity deficit u_s^i under pressure gradient has a Gaussian distribution, but with different normalised maximum velocity deficit $C^i(x)$ and wake width $\sigma^i(x)$ from its counterpart under ZPG (Shamsoddin & Porté-Agel 2018*a*). Therefore, u_s^i

and u_w^i for WT_i can be expressed as:

$$u_s^i(x, y, z) = u_b^i(x) C^i(x) \exp\left(-\frac{(y - y_i)^2 + (z - z_i)^2}{2\sigma^i(x)^2}\right), \tag{2.13}$$

$$u_w^i(x, y, z) = u_b^i(x) \left[1 - C^i(x) \exp\left(-\frac{(y - y_i)^2 + (z - z_i)^2}{2\sigma^i(x)^2}\right)\right]. \tag{2.14}$$

We give $C^i(x)$ and $\sigma^i(x)$ in § 2.2, and for now they are assumed to be known. The first term on the right-hand side of (2.12) can be linearised by introducing a convection velocity $u_c^i(x)$ (Zong & Porté-Agel 2020), and it can be given analytically as

$$u_c^i(x) = \frac{\iint u_w^i(x, y, z)[u_b^i(x) - u_w^i(x, y, z)] \, \mathrm{d}y \, \mathrm{d}z}{\iint [u_b^i(x) - u_w^i(x, y, z)] \, \mathrm{d}y \, \mathrm{d}z} = u_b^i(x)\left(1 - \frac{C^i(x)}{2}\right). \tag{2.15}$$

Therefore, the expression for the thrust of WT_i under pressure gradient can be rewritten as

$$\frac{T_i}{\rho} = \underbrace{u_c^i(x) \iint [u_b^i(x) - u_w^i(x, y, z)] \, \mathrm{d}y \, \mathrm{d}z}_{T_{MD}^i(x)} + \underbrace{\iint \int_{x_i - \delta x}^{x} \frac{\mathrm{d}U_b(x')}{\mathrm{d}x'} u_s^i(x', y, z) \, \mathrm{d}x' \, \mathrm{d}y \, \mathrm{d}z}_{T_{\mathfrak{p}}^i(x)}. \tag{2.16}$$

This equation indicates that for WT_i operating under pressure gradient, its thrust can be decomposed into two parts: the linearised momentum deficit flux T_{MD}^i and the integral of $\mathfrak{p}^i(x, y, z)$ (i.e. $T_{\mathfrak{p}}^i$), which is related to pressure gradient. In the derivation of (2.12) and (2.16), we have made some assumptions, such as the utilisation of the modified momentum deficit and the substitution of U_w^{i-1} by $u_b^i(x)$. However, these simplifications only lead to negligible errors based on the comparison between the modelled wind turbine thrust and LES results shown in § 4, indicating that these assumptions are reasonable.

2.1.4. *PG-IMCM superposition method*

Substituting (2.16) into (2.7) yields

$$\iint U_w(x, y, z)[U_b(x) - U_w(x, y, z)] \, \mathrm{d}y \, \mathrm{d}z$$

$$= \sum_{i \in B} u_c^i(x) \iint [u_b^i(x) - u_w^i(x, y, z)] \, \mathrm{d}y \, \mathrm{d}z$$

$$+ \sum_{i \in B} \iint \underbrace{\int_{x_i - \delta x}^{x} \frac{\mathrm{d}U_b(x')}{\mathrm{d}x'} u_s^i(x', y, z) \, \mathrm{d}x'}_{\mathfrak{p}^i(x, y, z)} \, \mathrm{d}y \, \mathrm{d}z$$

$$- \iint \underbrace{\int_{x_0}^{x} \frac{\mathrm{d}U_b(x')}{\mathrm{d}x'} U_s(x', y, z) \, \mathrm{d}x'}_{\mathfrak{P}(x, y, z)} \, \mathrm{d}y \, \mathrm{d}z. \tag{2.17}$$

Analogous to (2.15), we can define the combined convective velocity $U_c(x)$ to linearise the above equation:

$$U_c(x) = \frac{\iint U_w(x, y, z) U_s(x, y, z) \, \mathrm{d}y \, \mathrm{d}z}{\iint U_s(x, y, z) \, \mathrm{d}y \, \mathrm{d}z}. \tag{2.18}$$

Finally, we can obtain the analytical expression for wind-farm velocity deficit U_s under pressure gradient:

$$\text{PG-IMCM:} \quad U_s(x, y, z) = \underbrace{\sum_{i \in B} \frac{u_c^i(x)}{U_c(x)} u_s^i(x, y, z)}_{U_{s,LWS}} + \underbrace{\sum_{i \in B} \frac{\mathfrak{p}^i(x, y, z)}{U_c(x)}}_{U_{s,\mathfrak{p}}} - \underbrace{\frac{\mathfrak{P}(x, y, z)}{U_c(x)}}_{U_{s,\mathfrak{P}}}. \tag{2.19}$$

It can be seen that the wind-farm flow velocity deficit under pressure gradient consists of three terms. The first term is the linear-weighted sum of individual wake velocity deficits; the second term is the sum of $\mathfrak{p}^i$ divided by $U_c(x)$, whereas the third term is $\mathfrak{P}$ divided by $U_c(x)$. Here, we denote them as $U_{s,LWS}$, $U_{s,\mathfrak{p}}$ and $U_{s,\mathfrak{P}}$, respectively. Since the derivation of this superposition method is motivated by the IMCM method and is applicable to different pressure gradient conditions, we denote it as PG-IMCM here.

Equation (2.19) will have the exact solution of $U_s = u_s^1$ when $N = 1$, which is essentially the single-wake model under pressure gradient. In addition, (2.19) will be the same as IMCM (1.6) under the ZPG condition, i.e. $\mathrm{d}U_b(x)/\mathrm{d}x = 0$. Therefore, our proposed model can be viewed as a generalisation of the IMCM method under pressure gradient.

Similar to the IMCM method, this model also requires an iterative method (Zong & Porté-Agel 2020). First, we can give an initial guess of U_c based on the maximum value of u_c^i at different streamwise locations, and U_s can be calculated using (2.19). Then U_s can be substituted into (2.18) to update U_c. Finally, we can repeat the procedures until a certain criterion is reached. It should be noted that we compute the integral in the second and third terms by setting the upper limit of x' as $x - \Delta x$, where Δx is the grid size for numerical integration. In addition, the lower limit of x' in $\mathfrak{p}^i$ is $x_i - \Delta x$. This approximation will only have negligible error for small values of Δx. A step-by-step procedure of the PG-IMCM model is given in Appendix A.

2.2. *Wind-turbine wake models under pressure gradient*

The wake model under pressure gradient has been given as (2.13) and (2.14) in § 2.1.3, but with the maximum normalised velocity deficit $C^i(x)$ and wake width $\sigma^i(x)$ left to be determined. Here $C^i(x)$ can be solved through an ODE or its asymptotic solution (Shamsoddin & Porté-Agel 2018a). In this study, we use the asymptotic solution of the ODE to calculate $C^i(x)$ for its low computational cost and ease of use. It has been shown that, compared with the ODE, the asymptotic solution only has some errors in the near-wake region, whereas it can capture the influence of pressure gradient on the far-wake recovery very well (Shamsoddin & Porté-Agel 2018a). We also compared the ODE solution with its asymptotic solution under different atmospheric states in Appendix B.1, and it has been shown that the mean absolute percentage error between these two solutions is within 5 %, supporting that our choice of the asymptotic solution has a comparable prediction accuracy. The wake width $\sigma^i(x)$ under pressure gradient is determined through an invariant ratio $\lambda_0^i(x)$, which is defined based on the maximum normalised velocity

deficit $C_0^i(x)$ and wake width $\sigma_0^i(x)$ under the ZPG condition. The maximum normalised velocity deficit $C^i(x)$ and wake width $\sigma^i(x)$ of WT_i under pressure gradient can be written as follows (Shamsoddin & Porté-Agel 2018*b*):

$$C^i(x) = C_0^i(x) \left(\frac{u_0^i}{u_b^i(x)} \right)^{5/3}, \quad \sigma^i(x) = \frac{u_b^i(x)}{\lambda_0^i(x)} C^i(x), \tag{2.20a,b}$$

where u_0^i is $u_b^i(x_i)$. In addition, the invariant ratio $\lambda_0^i(x)$ under pressure gradient is given as

$$\frac{u_0^i C_0^i(x)}{\sigma_0^i(x)} = \lambda_0^i(x) = \frac{u_b^i(x) C^i(x)}{\sigma^i(x)}. \tag{2.21}$$

To calculate $C^i(x)$ and $\sigma^i(x)$, $C_0^i(x)$ and $\lambda_0^i(x)$ must be given at first. Here, we use the well-known Gaussian wake model (Bastankhah & Porté-Agel 2014) to calculate $C_0^i(x)$ as follows:

$$C_0^i(x) = \left[1 - \sqrt{1 - \frac{C_T^i}{8(\sigma_0^i(x)/D)^2}} \right] \mathcal{H}(x - x_i), \tag{2.22}$$

where C_T^i is the thrust coefficient of WT_i and the Heaviside step function $\mathcal{H}(x)$ is used here to ensure that wind-turbine wakes only influence the downstream region. To partially characterise the influence of the wind-rotor-induced pressure gradient in the near-wake region, the thrust coefficient can be rewritten in the form of the error function $C_T^i(x) = C_T^i[1 + \text{erf}((x - x_i)/D)]/2(x_i \leq x < x_i + 2D)$, according to Shapiro, Gayme & Meneveau (2018) and Zong & Porté-Agel (2020). $\sigma_0^i(x)$ is the standard deviation of the Gaussian wake profile of WT_i, and its empirical expression is written as follows (Zong & Porté-Agel 2020):

$$\frac{\sigma_0^i(x)}{D} = 0.35 + k_w^i \ln \left[1 + \exp \left(\frac{x - x_i - x_{th}^i}{D} \right) \right], \tag{2.23}$$

where k_w^i is the wake growth rate of WT_i, and it can be determined based on its inflow turbulence intensity I_u^i through the relationship $k_w^i = 0.38I_u^i + 0.004$ (Niayifar & Porté-Agel 2016). It should be noted that this expression is only applicable to the condition of $0.06 < I_u^i < 0.15$, $C_T^i \approx 0.8$. However, there is a big chance that $I_u^i > 0.15$ on the leeward side. We use $k_w^i = 0.26I_u^i$ under this condition (Teng & Markfort 2020). This empirical expression has been validated by Vahidi & Porté-Agel (2022) that it has a higher accuracy over $k_w^i = 0.38I_u^i + 0.004$ when the inflow turbulence intensity is high. In other words, we use a piecewise function to determine k_w^i.

The near-wake length x_{th}^i is modelled according to Bastankhah & Porté-Agel (2016) and Carbajo Fuertes, Markfort & Porté-Agel (2018) under the ZPG condition. Although it has been shown that pressure gradient influences the near-wake length to some extent, the sensitivity analysis presented in Appendix B.2 shows that using the model under the ZPG condition only leads to negligible differences in the calculation of x_{th}^i in comparison with the model proposed by Dar *et al.* (2023). Hence, we use the model under the ZPG condition for its low computational cost and simplicity of implementation.

The inflow turbulence intensity I_u^i is modelled as $\sqrt{I_b^2 + (\Delta I_u^i)^2}$, where I_b is the ambient streamwise turbulence intensity and ΔI_u^i is the added streamwise turbulence intensity at the

rotor plane for WT_i, which may be induced by multiple wind-turbine wakes similar to the velocity deficit. Here we define the added turbulence intensity induced by WT_j at the rotor plane of WT_i as $\delta I_u^{j \to i}$, which can be calculated by the three-dimensional Gaussian model proposed by Ishihara & Qian (2018). To calculate ΔI_u^i in the merged wake region, we resort to the maximum superposition method expressed as $\Delta I_u^i = \max_{j=1}^{i-1} \delta I_u^{j \to i}$ (Niayifar & Porté-Agel 2016), for more details about the superposition of the turbulence intensity, please refer to Li *et al.* (2023). It is noteworthy that the added turbulence intensity model is under the ZPG condition, which is also adopted by Dar & Porté-Agel (2024). Although pressure gradient may influence the production of turbulence intensity, developing such a model needs further research.

After obtaining the maximum velocity deficit $C_0^i(x)$ and wake width $\sigma_0^i(x)$ under the ZPG condition, $\lambda_0^i(x)$ can be obtained by (2.21). Substituting $\lambda_0^i(x)$ into (2.20), it is easy to know that

$$\sigma^i(x) = \sigma_0^i(x) \left(\frac{u_0^i}{u_b^i(x)} \right)^{2/3}. \tag{2.24}$$

As shown by (2.20) and (2.24), $C^i(x)$ and $\sigma^i(x)$ can be expressed directly by its counterpart under the ZPG condition and the base flow variation. Under the FPG condition, u_0^i will be less than $u_b^i(x)$, so both $C^i(x)$ and $\sigma^i(x)$ will lower than its counterpart under the ZPG condition, indicating a faster wake recovery, and *vice versa* under the APG condition. By substituting these two variables into (2.13) and (2.14), the wake velocity deficit and wake velocity under pressure gradient can be obtained.

2.3. *A simplified form of PG-IMCM*

Based on the previous two subsections, we have presented the complete form and implementation details of the PG-IMCM method, which is summarised in Appendix A. What makes the PG-IMCM method difficult to implement and time-consuming to calculate is that the last two terms in (2.19) are integral quantities. Therefore, it is of practical interest for us to investigate the magnitude of these terms and to see whether they can be simplified. For instance, if the sum of the last two terms is small enough compared with $U_{s,LWS}$, they can be neglected, resulting in a much simpler and computationally effective form. However, it is difficult for us to prove the assumption theoretically. Therefore, we first make a simple order-of-magnitude analysis of the sum of the last two terms in (2.19), which can be rewritten as

$$\Delta U_p = U_{s,\mathfrak{p}} - U_{s,\mathfrak{P}} = \frac{\sum_{i \in B} \mathfrak{p}^i - \mathfrak{P}}{U_c(x)} = \frac{1}{U_c(x)} \int_{x_0}^x \frac{\mathrm{d}U_b(x')}{\mathrm{d}x'} \left(\sum_{i \in B} u_s^i - U_s \right) \mathrm{d}x', \tag{2.25}$$

where $\sum_{i \in B} u_s^i$ represents the sum of individual velocity deficits using the local linear superposition method. In fact, the term in parentheses is the difference between the local linear superposition method and the PG-IMCM method, which is denoted as ΔU_s. By definition, it is easy to know that the combined convective velocity $U_c(x)$ has the same order as the base flow $U_b(x)$. If we assume that the base flow has a linear speed-up ratio γ,

Description	Values
Wind-farm configuration:	
Number of wind turbines	$N = 2, 3, \ldots, 8$
Turbine thrust coefficient	$C_T = 0.8$
Streamwise spacing	$S_x = 4D, 6D, 8D$
Atmospheric state:	
Normalised speed-up ratio	$c = -0.03, -0.02, \ldots, 0.03$
Ambient turbulence intensity	$I_b = 0.03, 0.05, \ldots, 0.15$

Table 1. Case set-up for the sensitivity study of the PG-IMCM method.

i.e. $dU_b/dx = \gamma$, we can obtain

$$\Delta U_p \sim \frac{\gamma(x - x_0)}{U_b(x)} \underbrace{\frac{1}{x - x_0} \int_{x_0}^{x} \Delta U_s \, dx'}_{\overline{\Delta U_s}}, \tag{2.26}$$

where $\overline{\Delta U_s}$ is the streamwise-averaged ΔU_s. In general, the wind speed variation $\gamma(x - x_0)$ within the wind farm caused by pressure gradient has the same order as the base flow $U_b(x)$. Therefore, $\Delta U_p \sim \overline{\Delta U_s}$. Although it has been shown that $\overline{\Delta U_s} \approx 0$ under the ZPG condition (Zong & Porté-Agel 2020), there is no generalised magnitude estimation applicable to FPG and APG conditions. Consequently, it is infeasible for us to analyse the magnitude of ΔU_p directly. Moreover, it is incomplete that we only know the magnitude of ΔU_p since whether we can neglect it depends on its relative magnitude to $U_{s,LWS}$. To this end, we further resort to a model sensitivity analysis under different wind-farm configurations and atmospheric states, which are typical of wind farm operational conditions under pressure gradient, as presented in table 1.

Specifically, we consider the aligned wind farm layout and all wind turbines have the same thrust coefficient $C_T = 0.8$. The base flow is modelled as a piecewise function:

$$U_b(x) = \begin{cases} U_{b0}[1 + c(x - x_1)/D], & c \geq 0, \\ U_{b0}[5 + c(x - x_1)/D], & c < 0, \end{cases} \tag{2.27}$$

where x_1 is the streamwise location of the first wind turbine, U_{b0} is the inflow velocity at x_1 and $c = \gamma D/U_{b0}$ is the normalised speed-up ratio. When $c < 0$, the inflow velocity is set to $5U_{b0}$ to prevent $U_b(x) < 0$ at farther downstream, which is unphysical. By systematically varying the number of wind turbines N, streamwise spacing S_x, normalised speed-up ratio c and ambient turbulence intensity I_b, the mean relative percentage of (2.25) to $U_{s,LWS}$ is quantified, which is defined as the streamwise-averaged absolute ratio of (2.25) to $U_{s,LWS}$ at the wake centreline for each case:

$$MRP_p = \frac{100\%}{x_N + S_x - x_1} \int_{x_1}^{x_N + S_x} \frac{|\Delta U_p|}{U_{s,LWS}} \, dx, \tag{2.28}$$

where x_N is the streamwise location of the last wind turbine.

Overall, the averaged $\overline{MRP_p}$ for all the cases is only about 0.4 %, indicating that neglect of the last two terms in the complete form will only lead to negligible error. Moreover, this implies that the local linear superposition method under pressure gradient has a very

999 A27-14

similar performance to the PG-IMCM method, as discussed later in § 5.2. Based on this analysis, we can provide a simplified form of PG-IMCM as follows:

$$\text{PG-IMCM-S:} \quad U_s(x, y, z) \approx \sum_{i \in B} \frac{u_c^i(x)}{U_c(x)} u_s^i(x, y, z). \tag{2.29}$$

As a simplified form of PG-IMCM, we denote it as PG-IMCM-S, and its calculation procedure is very similar to the PG-IMCM method, which is also given in Appendix A. It should be noted that PG-IMCM-S has the same form as Zong & Porté-Agel (2020), but the single turbine wake quantities $u_c^i(x)$ and $u_s^i(x)$ are redefined to account for the influence of pressure gradient, as detailed in § 2.1.3. For the first time, our derivation and analysis reveal the similarities and differences between the momentum-conserving wake superposition methods under different pressure gradient conditions and form the basis for a unified framework. On the other hand, based on the form of PG-IMCM-S, it is demonstrated that wake superposition under pressure gradient does not need to explicitly account for the effect of pressure gradient, whereas it is necessary to account for the influence of pressure gradient on background wind speed and wake recovery when calculating individual velocity deficits. These implications pave the way for extending the empirical superposition principles under pressure gradient in § 5.

Although PG-IMCM and PG-IMCM-S have very close prediction results, their physical meanings differ significantly. PG-IMCM is the direct consequence by linearising the integral momentum-conserving equation, which has a solid theoretical foundation. Specifically, the integral of the product of the wind-farm convection velocity with the sum of the first two terms on the right-hand side of (2.19) is the total thrust of the wind farm, whereas the other term represents the influence of background pressure gradient. In contrast, PG-IMCM-S has limited physical insights and is only an indirect result of the momentum conservation equation. One advantage of the PG-IMCM-S method is that it is easy to implement and computationally effective.

The inputs of the model consist of environment variables and wind turbine variables. The former includes the base flow $U_b(x)$ and ambient streamwise turbulence intensity I_b, whereas the latter consists of the rotor centre coordinates (x_i, y_i, z_i), thrust coefficient C_T^i and rotor diameter D of WT_i. The output of the model is the wind-farm velocity deficit $U_s(x, y, z)$. In this study, U_b is extracted directly from the main computational domain without wind turbines. For the wind farm layout optimisation in complex terrain, the background flow field can be modelled by using some computational fluid dynamics (CFD) tools, such as WAsP and WindSim, for a number of inflow wind direction sectors (Brogna *et al.* 2020). In addition, it can be modelled through some empirical functions (Sun, Yang & Gao 2023) or linearised perturbation equations (Hunt, Leibovich & Richards 1988; Shamsoddin & Porté-Agel 2018*b*) under some simple terrains (such as ramps and hills with gentle slopes).

3. LES methodology and case set-up

In this study, we use LES to simulate the evolution of wind-turbine wakes under different pressure gradients, which is used to compare and validate the performance of the proposed WFFAMs. Pressure gradient is simulated by complex terrains, which are modelled via the wall-modelled immersed boundary method (IBM). LES methodology and the validation case set-up are given below.

3.1. *LES methodology*

Here, we utilise the pseudo-spectral solver LESGO for numerical simulation, which has been validated by wind tunnel experiments (e.g. Stevens, Martínez-Tossas & Meneveau 2018; Liu & Stevens 2020*b*; Zhang *et al.* 2022*b*) and widely adopted in the studies on wind turbines and wind-farm flows (Du *et al.* 2021; Ge *et al.* 2021; Ma *et al.* 2021; Zhang *et al.* 2021*a*; Du, Ge & Liu 2022, among others), atmospheric boundary layer over complex terrain (Liu & Stevens 2020*a*,*b*; Zhang *et al.* 2022*b*) as well as urban canopy flows (e.g. Ge *et al.* 2020; Fan *et al.* 2021; Ge *et al.* 2021; Zhang *et al.* 2021*a*,*b*, 2022*a*). LES solves the spatially filtered unsteady incompressible Navier–Stokes equations, where the continuity and momentum equations are written as

$$\frac{\partial \tilde{u}_i}{\partial x_i} = 0, \tag{3.1}$$

$$\frac{\partial \tilde{u}_i}{\partial t} + \tilde{u}_j \frac{\partial \tilde{u}_i}{\partial x_j} = -\frac{\partial \tilde{p}^*}{\partial x_i} - \frac{\partial \tau_{ij}^d}{\partial x_j} - \frac{f}{\rho}. \tag{3.2}$$

Here, $\tilde{}$ is the filter at the spatial scale Δ, t is time, $\tilde{u}_i$ is the filtered velocity in the i-direction (with $i = 1$, 2 and 3 corresponding to the streamwise (x), spanwise (y) and vertical (z) directions, respectively), $\tilde{p}^* = \tilde{p}/\rho + 1/3\tau_{kk}$ is the modified pressure and τ_{ij}^d is the deviatoric part of the sub-grid scale stress tensor, which is modelled by the Smagorinsky model with wall damping function (Bou-Zeid, Meneveau & Parlange 2005). Since the Reynolds number based on the rated wind speed ($\sim$10 m s^{-1}) and rotor diameter ($\sim$100 m) is $\sim$10^7, the effect of the viscous term in the momentum equation is neglected. Here f is the external force, and it can originate from different sources as follows:

$$f = f_p + f_t - f_{IB}, \tag{3.3}$$

where f_p is the constant pressure gradient that drives the flow, f_t represents the actuator force induced by the wind turbine and f_{IB} is the body force that needs to be enforced to ensure the grid velocity is zero in the solid region.

Here, we adopt the wall-modelled IBM developed by Liu & Stevens (2020*b*), which is a simplified version of the three-step level-set method proposed by Chester, Meneveau & Parlange (2007). This method introduces a signed distance function $\phi(x)$, and the computational domain is divided into solid region, fluid region and fluid–solid interface region based on $\phi(x)$ at first. Then, different treatments are used for different regions; that is, the velocity at the grid of the solid region is enforced to zero, and the sub-grid scale stress of the fluid–solid interface region is calculated using the wall model, whereas no further treatment is done to the grid in the fluid region. For more details about the wall-modelled IBM, please refer to Liu & Stevens (2020*b*).

Wind turbines are modelled using the filtered actuator disk model (Shapiro, Gayme & Meneveau 2019). Based on the one-dimensional momentum theory, the total thrust F_t can be expressed as

$$F_t = \frac{1}{2}\rho A C_T U_\infty^2 = \frac{1}{2}\rho A C_T \frac{U_d^2}{(1-a)^2}, \tag{3.4}$$

where U_∞ is the freestream inflow wind speed, A is the swept area of the wind rotor, ρ is the air density, C_T is the thrust coefficient, a is the axial induction factor and U_d is the rotor-averaged velocity. Finally, the total thrust F_t is distributed to the computation grids to obtain f_t according to the Gaussian-filtered indicator function $\Re(x)$. For more details about the determination of $\Re(x)$, please refer to Shapiro *et al.* (2019).

Case	x_{ct}/D	L_u/D	L_d/D	H/D	x_T/D
FPG-CVW-WT	55	25	5	2.5	16, 24, 32, 40
FPG-CVW	55	25	5	2.5	—
APG-CCW-WT	55	25	5	−3.5	16, 24, 32, 40
APG-CCW	55	25	5	−3.5	—

Table 2. Overview of the ideal convex and concave channel cases. (CVW and CCW represent the convex and concave walls, respectively, and WT represents there are wind turbines in this case; x_T is the streamwise location of the rotor centre.)

Uniform grids are used in the horizontal direction, and a staggered Cartesian grid is used in the vertical direction. The pseudo-spectral method is used for the horizontal spatial discretisation. In the vertical direction, the second-order central finite difference method is adopted. For time advancement, the code uses the second-order accurate Adams–Bashforth method.

Note that the filter symbol is omitted hereafter for convenience. Although the pressure simulated in this study includes the trace of the sub-grid scale stress tensor, it is expected only to cause a small difference in the momentum balance and the Bernoulli equation (Bastankhah *et al.* 2021).

3.2. *Case set-up*

In general, convex (concave) topography will induce FPG (APG). To validate the performance of the proposed WFFAMs under pressure gradient, we set up two types of cases. One type is the ideal convex and concave channels consisting of symmetric upper and lower walls with respect to the centre plane of the channel (Shamsoddin & Porté-Agel 2018*a*), which can be used to simulate FPG and APG conditions, respectively. The surface equation $Z_l(x, y)$ of the lower wall has the following general cosine form:

$$
Z_l(x, y) = \begin{cases}
\dfrac{1}{2}H\left[1 + \cos\left(\dfrac{\pi}{2L_u}(x - x_{ct})\right)\right], & -2L_u \leq x - x_{ct} < 0, \\[2ex]
\dfrac{1}{2}H\left[1 + \cos\left(\dfrac{\pi}{2L_d}(x - x_{ct})\right)\right], & 0 \leq x - x_{ct} < 2L_d, \\[2ex]
0, & \text{otherwise,}
\end{cases}
\tag{3.5}
$$

where x_{ct} is the position of the channel throat, H is the height difference between the throat position and the horizontal ground, and L_u and L_d are the upstream and downstream half-lengths of the cosine functions, respectively. The corresponding expression for the upper wall is $Z_u(x, y) = 10D - Z_l(x, y)$. The detailed parameter settings are listed in table 2. In this condition, wind turbines are placed at the centre of the y–z plane of the computational domain, as shown in figure 4.

Another type of case consists of two linear ramps and one platform at the bottom (Dar *et al.* 2023; Dar & Porté-Agel 2024), as shown in figure 5. Wind turbines are placed at the same distance over the ground, and their rotors are perpendicular to the ramp. The hub height is the same as the rotor diameter. To facilitate the comparison between the proposed model and the ramp case, we define a local ramp coordinate following the slope of the ramp, whose origin is located in the rotor centre of the first wind turbine in the wind farm array, as shown in figure 5. This case setting is closer to the realistic engineering situation
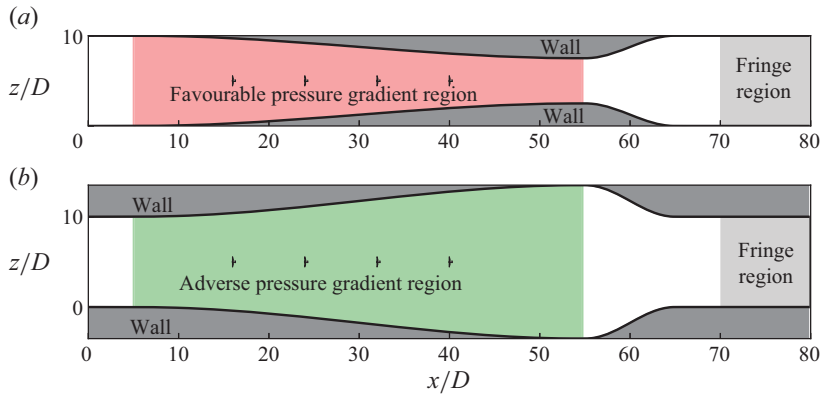
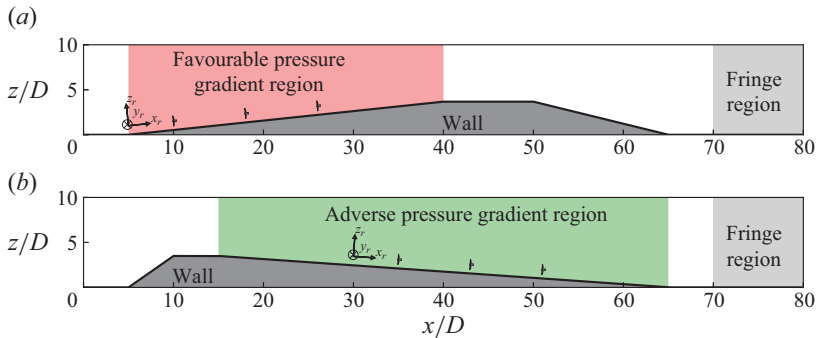Figure 4. Schematics of the computational domain for (*a*) FPG-CVW-WT and (*b*) APG-CCW-WT.

Figure 5. Schematics of the computational domain for (*a*) FPG-RAMP-WT and (*b*) APG-RAMP-WT.

than channel cases. The analytical expression of the ramp height $Z_r(x, y)$ is written as follows:

$$
Z_r(x, y) = \begin{cases}
H_r \left(\dfrac{x - x_w}{L_1} \right), & x_w \leq x < x_w + L_1, \\
H_r, & x_w + L_1 \leq x < x_w + L_1 + L_2, \\
H_r \left(1 - \dfrac{x - x_w - L_1 - L_2}{L_3} \right), & x_w + L_1 + L_2 \leq x < x_w + L_1 + L_2 + L_3, \\
0, & \text{otherwise},
\end{cases}
$$

(3.6)

where x_w is the starting location of the windward ramp, H_r is the height of the platform, L_2 is the length of the platform, and L_1 and L_3 are the projected lengths of the windward and leeward ramps, respectively. The detailed parameter settings are given in table 3.

It should be noted that although we made no assumptions about the wind-farm layout in the model derivation, we only simulated the aligned layout in the validation cases, which serves as a basis for verifying the wake superposition method (Zong & Porté-Agel 2020; Lanzilao & Meyers 2022; Dar & Porté-Agel 2024). In this case, the wake generated by different wind turbines will be fully merged, and the wake superposition is very complicated, providing a fair condition to test the performance of different superposition methods.

999 A27-18

Case	x_w/D	L_1/D	L_3/D	L_2/D	H_r/D	x_T/D
FPG-RAMP-WT	5	35	15	10	3.68	10, 18, 26
FPG-RAMP	5	35	15	10	3.68	—
APG-RAMP-WT	5	5	50	5	3.5	35, 43, 51
APG-RAMP	5	5	50	5	3.5	—

Table 3. Overview of the ramp cases.

The main computational domain for the FPG-CVW-WT, FPG-RAMP-WT and APG-RAMP-WT cases is set to $80D \times 12D \times 10D$. However, due to the setting of concave walls, the main computational domain for the APG-CCW-WT case is expanded to $80D \times 12D \times 17D$. The number of grids in both computational domains is $320 \times 120 \times 144$, which can ensure the rotor diameter is covered with about 10 points in both the spanwise and vertical directions. Such a grid resolution is fine enough for the actuator disk model to predict the velocity deficit in turbine wakes with reasonable accuracy (Wu & Porté-Agel 2011; Shamsoddin & Porté-Agel 2018*a,b*; Lin & Porté-Agel 2022). The thrust coefficient of all wind turbines is set to 0.8. In addition to the above four cases with wind turbines, four cases without wind turbines under the same condition are simulated in tables 2 and 3 to obtain the base flow, which is used as inputs to WFFAMs and to calculate the normalised velocity deficit. To overcome the streamwise periodicity and ensure a fully developed inflow to the main computational domain, we use the concurrent precursor method proposed by Stevens, Graham & Meneveau (2014), in which the flow field in the fringe region at the end of the main domain is blended with the ideal straight channel flow for the curved channel cases and half-channel flow for the ramp cases, whose domain size and grid size are the same as the main computational domain. The computational accuracy of the LES framework in these channel and half-channel flows has been tested in several validation studies (e.g. Shamsoddin & Porté-Agel 2018*a,b*; Liu & Stevens 2020*b*; Zhang *et al.* 2022*b*). The surface roughness of the ground and topography are both 0.001*D*, a typical value of onshore topography.

4. Model validation

In this section, we compare the prediction accuracy of PG-IMCM and its simplified form based on LES results. To make a more straightforward comparison, we compute the normalised velocity deficit as follows:

$$\frac{U_s(x, y, z)}{U_{b0}} = \frac{U_{bg}(x, y, z) - U_w(x, y, z)}{U_{b0}}, \tag{4.1}$$

where U_{bg} and U_w are the time-averaged background flow velocity and wind-farm flow velocity, respectively, and U_{b0} is the hub-height spanwise-averaged $\langle U_{bg} \rangle_y$ at the streamwise location of the first wind turbine for each validation case. The model input $U_b(x)$ is the hub-height spanwise-averaged $\langle U_{bg} \rangle_y$.

4.1. *Validation of the momentum-conserving method under FPG*

In this subsection, we validate the performance of the momentum-conserving method under FPG. Under FPG condition, the pressure decreases streamwise, and the background
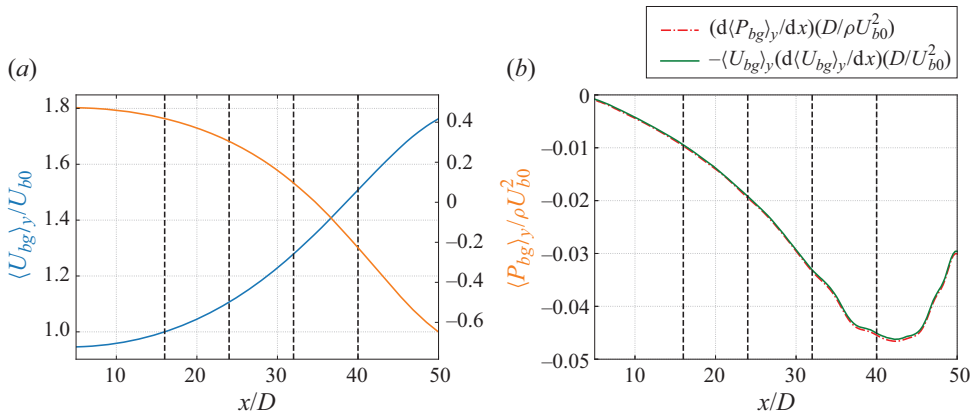
Figure 6. Streamwise variations of the normalised spanwise-averaged (*a*) velocity and pressure and (*b*) kinetic energy gradient and pressure gradient at hub height for the FPG-CVW case. (Vertical black dashed lines represent the locations of wind turbines.)
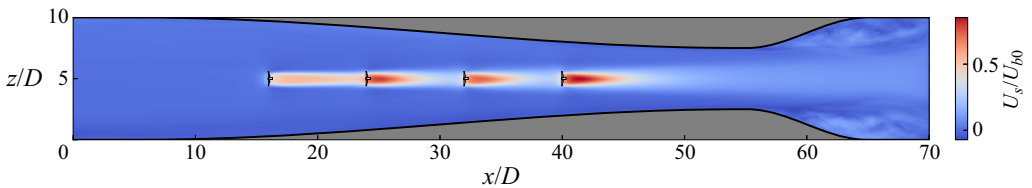

Figure 7. Contours of the normalised velocity deficit at the *x–z* rotor symmetry plane for the FPG-CVW-WT case.

wind velocity increases, which is beneficial to the wake recovery (Shamsoddin & Porté-Agel 2018*a*).

4.1.1. *Validation of results based on the FPG-CVW-WT case*

Figure 6(*a*) shows the streamwise variations of the normalised spanwise-averaged velocity and pressure at hub height for the FPG-CVW case. It can be seen that the pressure decreases as the streamwise distance increases, and the wind speed increases gradually, indicating that we have successfully simulated the ideal FPG case. The mean base flow gradient $\overline{\mathrm{d}U_b/\mathrm{d}x}$ from $16D$ to $50D$ is about $0.0224 U_{b0}/D$. In addition, figure 6(*b*) shows the streamwise variations of the normalised spanwise-averaged kinetic energy gradient and pressure gradient at hub height for the FPG-CVW case. We can see that these two curves nearly coincide, indicating that the pressure and wind speed satisfy the Bernoulli equation $\langle P_{bg}\rangle_y/\rho + 1/2\langle U_{bg}\rangle_y^2 = \mathrm{const.}$. Therefore, this case meets the applicability of the wake model and PG-IMCM superposition method under pressure gradient, which is necessary for a fair comparison.

Figure 7 presents the contours of the normalised velocity deficit at the *x–z* rotor symmetry plane. It can be seen that the velocity deficit downstream of the first wind turbine is the smallest, and its recovery is the slowest, whereas the wake velocity deficit downstream of the last wind turbine is the largest. In addition, the second and third wind turbines have similar wake velocity deficit and recovery rates.

Whether the maximum velocity deficit at hub height $U_{s,max}$ in the merged wake region can be accurately predicted is one of the crucial metrics for the assessment of superposition
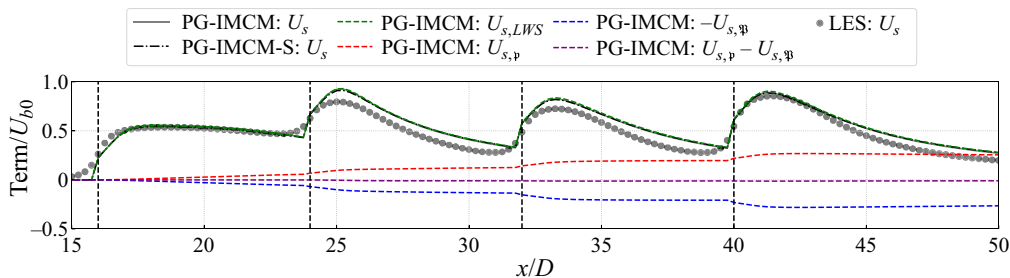
999 A27-20

Figure 8. Model prediction of $U_{s,max}/U_{b0}$ in comparison with LES for the FPG-CVW-WT case. (Vertical black dashed lines represent the locations of wind turbines.)

methods. Figure 8 shows the comparison of $U_{s,max}/U_{b0}$ obtained by PG-IMCM and LES for the FPG-CVW-WT case. In addition to the total velocity deficit, its decomposition terms (i.e. $U_{s,LWS}$, $U_{s,\mathfrak{p}}$ and $-U_{s,\mathfrak{P}}$) are also presented in the figure. As expected, the sum of the pressure correction term induced by individual velocity deficits $\sum_{i \in B} \mathfrak{p}^i$ and the pressure correction term induced by total velocity deficit $-\mathfrak{P}$ accumulate with the downstream distance, as they are integral quantities. When divided by the combined velocity U_c, they become $U_{s,\mathfrak{p}}$ and $-U_{s,\mathfrak{P}}$, whose variation is very similar to the sum of four stair-step functions located at the wind-turbine locations. As expected, they have opposite symbols but very close magnitudes, and the mean absolute value of their sum is only about $0.008 U_{b0}$. Therefore, the sum of these two terms can be neglected, and the prediction result of the PG-IMCM method can be viewed as the linear-weighted sum of individual velocity deficits. In addition, we also present the prediction results of PG-IMCM-S, which is virtually identical with PG-IMCM, further validating our simplification based on the sensitivity study. Overall, PG-IMCM and its simplified form have a good prediction over $U_{s,max}$, only with a slight overestimation in the merged wake region.

Furthermore, we are also concerned about the prediction of velocity deficit profiles by WFFAMs in practical applications since it is closely related to the power calculation of wind turbines. Figure 9 compares the spanwise velocity deficit profiles at hub height obtained by PG-IMCM, PG-IMCM-S and LES downstream of each wind turbine for the FPG-CVW-WT case. Similar to figure 8, a term-by-term comparison is also presented. At first, we can see that $U_{s,\mathfrak{p}}$ and $-U_{s,\mathfrak{P}}$ have a near Gaussian distribution, and their sum can be neglected. The prediction of PG-IMCM and its simplified form is nearly collapsed at each radial location, similar to the rotor centre. Overall, the PG-IMCM method and its simplified form have a good prediction accuracy over the profiles, with a slight overestimation in the rotor centre region.

LES results can not only serve as a baseline for the model validation but also can be used to examine some assumptions in the derivation of the PG-IMCM method. Here, we compare the wind turbine thrust modelling (2.16) based on the single-wake quantities with LES results, as shown in figure 10. It can be seen that the wind thrust modelling can represent the variation and magnitude of the total thrust in the control volume B very well. The sum of momentum deficits of stand-alone turbine wakes $\sum_{i \in B} T^i_{MD}$ under FPG condition is less than the total thrust, whereas the sum of pressure correction terms $\sum_{i \in B} T^i_{\mathfrak{p}}$ makes up for this deficit, finally resulting in a good prediction of the total thrust, which is an essential part of the PG-IMCM method. It should be noted that the slight underestimation in the near-wake region is related to the modified thrust coefficient within the downstream $2D$ region.
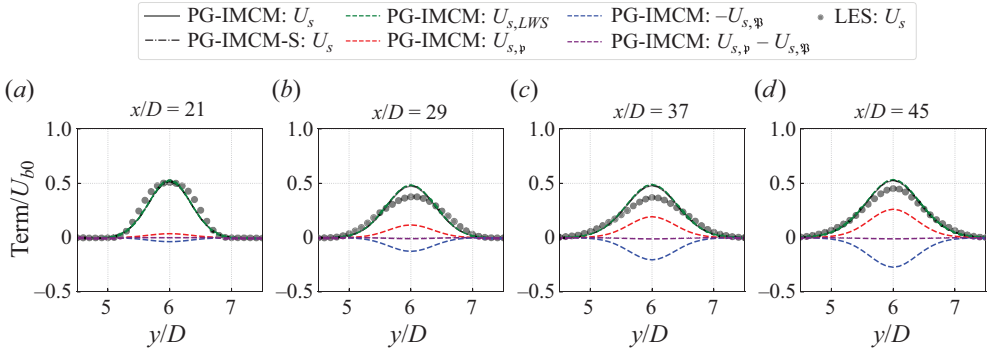
Figure 9. Model prediction of the spanwise velocity-deficit profiles at hub height downstream of each wind turbine in comparison with LES for the FPG-CVW-WT case.
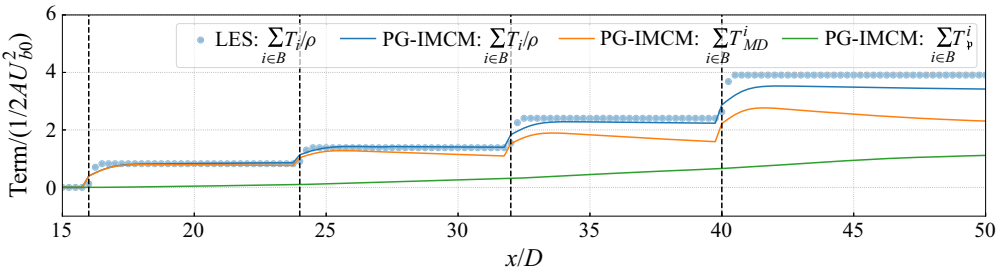

Figure 10. Comparison of the modelled wind-turbine thrust with LES for the FPG-CVW-WT case. (Vertical black dashed lines represent the locations of wind turbines.)

4.1.2. *Validation of results based on the FPG-RAMP-WT case*

The FPG-CVW-WT case is too ideal, leading to minimal wind shear and ambient streamwise turbulence intensity (about 2.3 %) in the rotor region, which does not represent the realistic atmospheric surface boundary layer with high wind shear and high turbulence intensity. Therefore, to further validate the applicability of the proposed momentum-conserving method under FPG condition, we set up the FPG-RAMP-WT case, as depicted in figure 5(*a*), which is closer to the realistic operation environment of the wind turbine. In this case, streamwise turbulence intensity at hub height is about 6 %. Because of the ramp, the flow has a streamwise component U_x and a vertical component U_z. Therefore, the velocity U used in the analysis of the FPG-RAMP-WT and APG-RAMP-WT cases is $\sqrt{U_x^2 + U_z^2}$.

Figure 11 shows the contours of the spanwise-averaged wind field and pressure for the FPG-RAMP case. It can be observed that the flow up the windward ramp evolves downstream approximately parallel to the surface and gradually accelerates before approaching the platform. The corresponding pressure gradually decreases, indicating that the FPG condition is successfully simulated through this set-up. The base flow has a nearly constant speed-up ratio above the windward ramp, and its mean value $\overline{\mathrm{d}U_b/\mathrm{d}x_r}$ from $0D$ to $26D$ is about $0.0215U_{b0}/D$. We also examined the kinetic energy gradient and pressure gradient at hub height for the FPG-RAMP case, and they still approximately conform to the Bernoulli equation. Here, we do not show them for brevity.
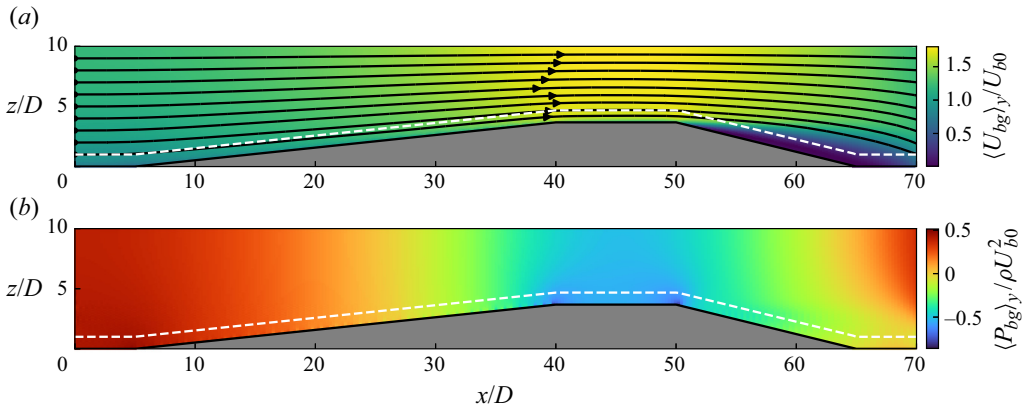
999 A27-22

(*a*)

(*b*)

Figure 11. Contours of the spanwise-averaged (*a*) wind field and (*b*) pressure for the FPG-RAMP case. (The white dashed line represents hub height, and black solid lines represent streamlines.)
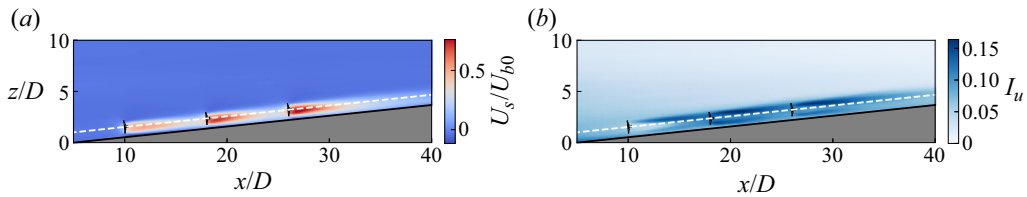
(*a*)   (*b*)

Figure 12. Contours of the (*a*) normalised velocity deficit and (*b*) streamwise turbulence intensity at the *x*–*z* rotor symmetry plane for the FPG-RAMP-WT case. (The white dashed line represents hub height.)

Figure 12 shows the contours of the normalised velocity deficit and streamwise turbulence intensity at the *x*–*z* rotor symmetry plane for the FPG-RAMP-WT case. We can see that the velocity deficit computed by LES has an obvious accumulation pattern in this case; that is, the wake velocity deficit of the first wind turbine is the smallest, whereas the wake velocity deficit downstream of the third wind turbine is the largest. As for the streamwise turbulence intensity, its magnitude in the wake of the first wind turbine is low, whereas its magnitude downstream of the second and third wind turbines is high, and their spatial distribution is quite similar. This finding is consistent with Li *et al.* (2023), who have studied the spatial distribution characteristics of the added streamwise turbulence intensity in the merged wake region of an aligned wind turbine array under the ZPG condition, indicating that the adoption of the maximum superposition method for the wake-added turbulence is reasonable.

Figures 13 and 14 show the comparison of $U_{s,max}/U_{b0}$ and the spanwise velocity deficit profiles at hub height obtained by the momentum-conserving WFFAMs and LES for the FPG-RAMP-WT case, respectively. The term-by-term comparison results are very similar to the FPG-CCW-WT case, thus not repeated here. Overall, the momentum-conserving methods show a remarkably high prediction accuracy in this case, further validating the accuracy of the proposed superposition method. A comparison of the modelled turbine thrust with LES results is further shown in figure 15. Similar to the results presented in figure 10, we can observe that the modelled turbine thrust agrees well with LES results, further confirming the validity of (2.16).

The term-by-term analysis of the proposed momentum-conserving method in the above two cases with different ambient turbulence intensity under FPG conditions confirms the
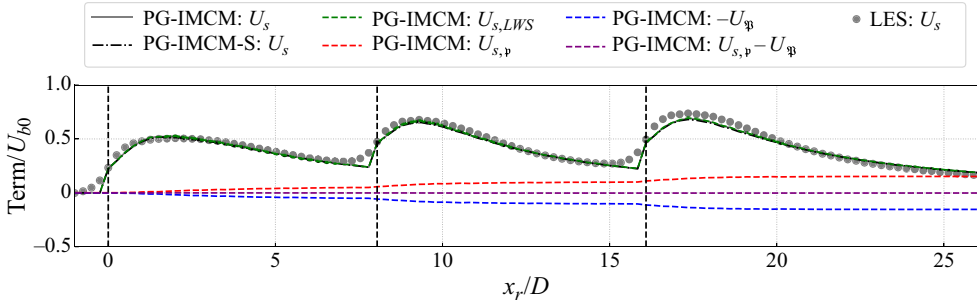
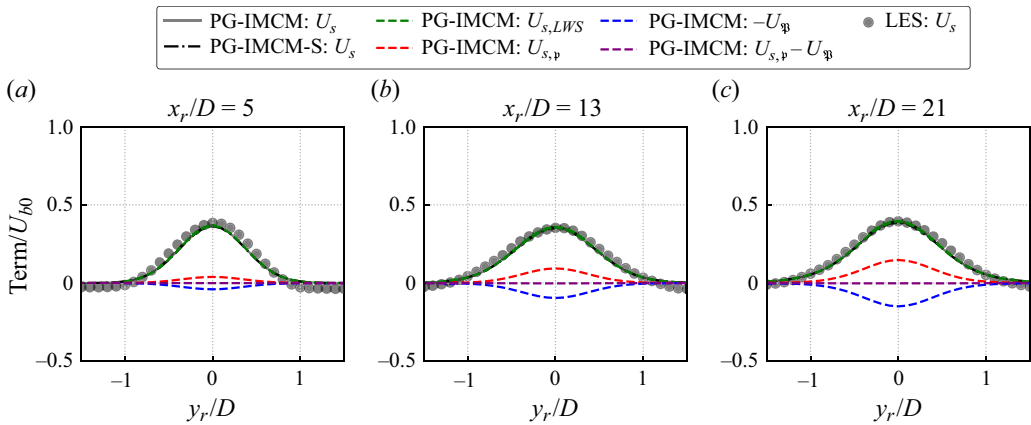Figure 13. Same as figure 8, but for the FPG-RAMP-WT case.

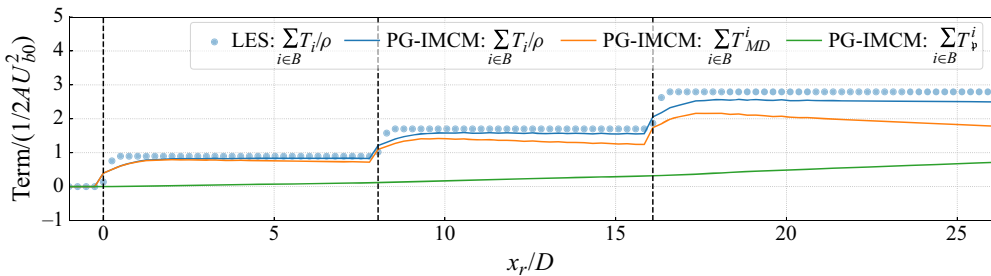Figure 14. Same as figure 9, but for the FPG-RAMP-WT case.

Figure 15. Same as figure 10, but for the FPG-RAMP-WT case.

validity of the linearised expression of the turbine thrust derived in § 2.1.3 and shows that our proposed model can predict the maximum velocity deficit and spanwise velocity deficit profiles at hub height very well.

Interestingly, the proposed methods have higher accuracy in the realistic ramp case than the ideal concave channel case. This may be attributed to two reasons. On the one hand, the ambient streamwise turbulence intensity is only 2.3 % in the ideal concave channel case, resulting in a much longer near-wake region. The velocity deficit profiles of the first turbine are closer to super-Gaussian, as depicted in figure 9(*a*). When we use the Gaussian profile, it will result in a more slender spanwise profile. On the other hand, the ideal curved channel
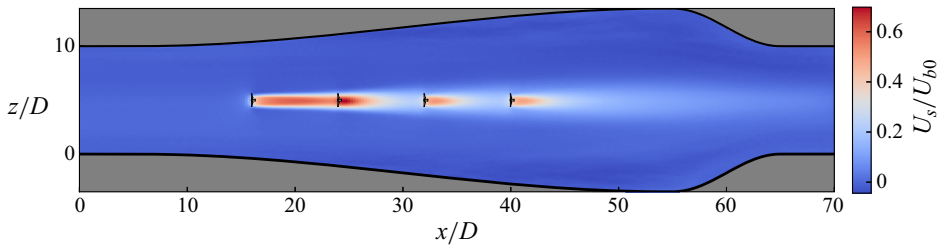
Figure 16. Same as figure 7, but for the APG-CCW-WT case.

cases may be out of the application range of some empirical relation of wake quantities, especially the wake growth rate. This is because this expression is obtained by curve-fitting based on the LES results and field measurements in the atmospheric boundary layer, which is characterised by the high wind shear and ambient turbulence intensity.

4.2. *Validation of the momentum-conserving method under APG*

In this subsection, we focus on the validation of the momentum-conserving method under APG. In contrast to the FPG condition, the pressure increases streamwise and the corresponding wind velocity decreases under the APG condition. Compared with the ZPG condition, the APG condition will make the wake recovery slower (Shamsoddin & Porté-Agel 2018*a*).

4.2.1. *Validation of results based on the APG-CCW-WT case*

The base flow has a nearly constant gradient in the region of interest, and the mean base flow gradient $\overline{\mathrm{d}U_b/\mathrm{d}x}$ from $16D$ to $50D$ is about $-0.0062U_{b0}/D$ for the APG-CCW case. The ambient turbulence intensity is about 2.5 %. In addition, we compare the normalised spanwise-averaged kinetic energy gradient and pressure gradient at hub height for the APG-CCW case, and they almost collapse, indicating that the case set-up satisfies the applicability of the wake model and the PG-IMCM superposition method. For brevity, we do not show them here. Figure 16 shows the contours of the normalised velocity deficit at the x–z rotor symmetry plane for the APG-CCW-WT case. It can be seen that the wake recovery is the slowest downstream of the first wind turbine. The wake velocity deficit downstream of the second wind turbine is the largest, and then it recovers very quickly. The wake velocity deficits and their recovery downstream of the third and fourth wind turbines are relatively similar. In this case, the spatial distribution of the merged wake velocity deficit is significantly different from that under ZPG and FPG conditions. The proposed momentum-conserving method cannot accurately predict the variations in the maximum velocity deficit in the merged wake region in this case, as shown in figure 17.

One possible explanation for this phenomenon is the combined effects of the low ambient turbulence intensity and APG, which stimulates the wake meandering behind the second wind turbine. Observations from various studies, such as Gupta & Wan (2019), Li, Dong & Yang (2022), Gambuzza & Ganapathisubramani (2023) and Messmer, Hölling & Peinke (2024), have supported the mechanism that wake meandering occurs in the far wake due to the amplification of upstream disturbances by shear flow instabilities, especially when the inflow's turbulence intensity is low. Moreover, the optimal perturbations are those large-scale (the same order as the turbine rotor) and low-frequency coherent eddies (Mao & Sørensen 2018). This is the situation for the second wind turbine, which is
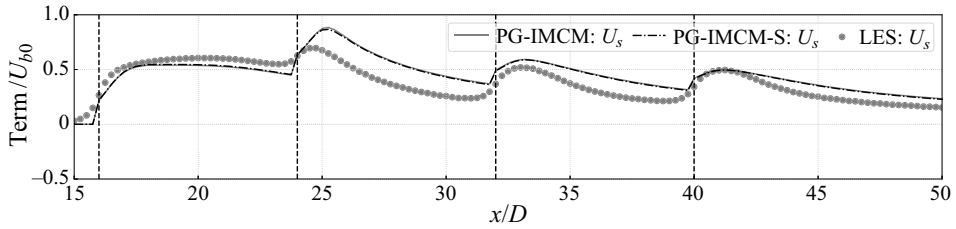
Figure 17. Model prediction of $U_{s,max}/U_{b0}$ in comparison with LES for the APG-CCW-WT case.

immersed in the wake of the first wind turbine. In this condition, the small perturbations in the far-wake region of the first turbine will be amplified significantly by the complex nonlinear dynamics, leading to enhanced wake recovery. As a result, the wake downstream of the second wind turbine recovers quickly and is in an unsteady physical process, which does not satisfy the applicability of existing wake models and their empirical expressions. A similar phenomenon has also been observed in the study on the influence of swells on the wake evolution of aligned wind turbines (Yang *et al.* 2022).

Although the same situation is also satisfied in the FPG-CVW-WT case, our model only has a slight underestimation of wake recovery, which may be related to the potential influence of pressure gradient on the wake meandering. In other words, the FPG condition will suppress the selective amplification, making the empirical expression of wake growth rate still applicable only with a minor error, whereas the APG condition will enhance this process, resulting in a high prediction error.

It should be noted that our explanation is a qualitative conjecture based on the simulation results. A quantitative analysis on the influence of pressure gradient on wake meandering, especially the selective amplification mechanism, is beyond the scope of the study, which is an interesting topic for future research.

Therefore, the misestimation of PG-IMCM in this case can be attributed to the invalidity of the stand-alone turbine wake model rather than the superposition method. No further comparison based on this case is given hereafter for brevity.

4.2.2. *Validation of results based on the APG-RAMP-WT case*

To solve the problems mentioned previously, we further set up a leeward ramp to simulate the APG condition with a high ambient turbulence intensity, as depicted in figure 5(*b*). The prediction results of the momentum-conserving method in this case are further compared and analysed.

At first, figure 18 shows the contours of the spanwise-averaged wind field and pressure for the APG-RAMP case. We can observe that the flow upper the leeward ramp evolves downstream nearly parallel to the surface and gradually decelerates before approaching the ground, and the corresponding pressure gradually increases. It indicates that the expected APG condition is successfully simulated. The base flow has a nearly constant gradient above the leeward ramp, and its mean value $\overline{dU_b/dx_r}$ from $0D$ to $26D$ is about $-0.0128U_{b0}/D$. Furthermore, we compare the kinetic energy gradient and pressure gradient at hub height for the APG-RAMP case. Similar to the FPG-RAMP case, they approximately satisfy the Bernoulli equation in the region of interest and meet the prerequisite of the wake model and the PG-IMCM superposition model under pressure gradient. For brevity, we do not show them here.
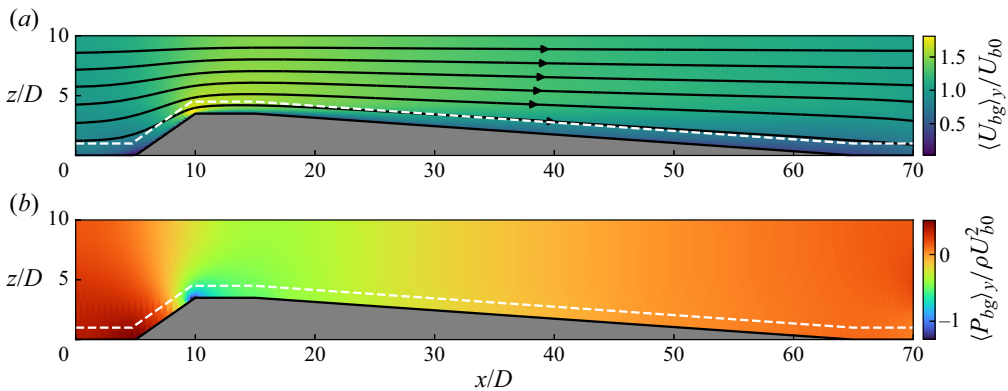
999 A27-26

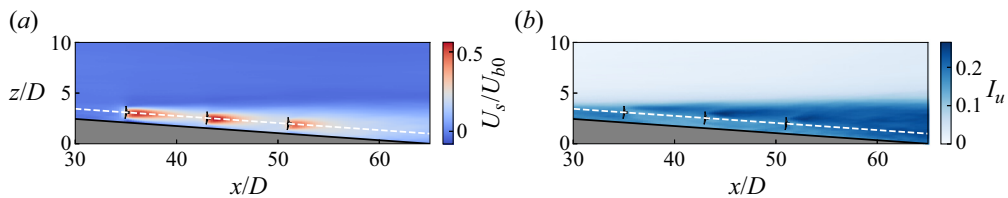Figure 18. Same as figure 11, but for the APG-RAMP case.

Figure 19. Same as figure 12, but for the APG-RAMP-WT case.

The contours of the normalised velocity deficit and streamwise turbulence intensity at the x–z rotor symmetry plane for the APG-RAMP-WT case are depicted in figure 19. In the upper region of the leeward ramp, the downslope flow affects the wind turbine, and the streamwise turbulence intensity at the location of WT_i is about 16 %. As a result, wind-turbine wakes recover very quickly. Figures 20 and 21 show the comparison of $U_{s,max}/U_{b0}$ and the spanwise velocity deficit profiles at hub height obtained by the momentum-conserving WFFAMs and LES for the APG-RAMP-WT case, respectively. Due to $\mathrm{d}U_b/\mathrm{d}x_r < 0$ under APG condition, $U_{s,\mathfrak{p}}$ is less than zero, whereas $-U_{s,\mathfrak{P}}$ is larger than zero, which is in contrast to the case under the FPG condition. These two terms have a relatively close absolute value, with the mean absolute value of their sum only about $0.004U_{b0}$. Hence, neglecting them only leads to negligible differences throughout the region of interest. The momentum-conserving method performs well in this case, validating the applicability of PG-IMCM and its simplified form under APG condition.

Figure 22 compares the cumulative turbine thrust modelled by (2.16) with LES results in this case. Different from the FPG condition, $\sum_{i \in B} T_{MD}^i$ under APG condition is larger than the thrust, whereas the pressure correction term $\sum_{i \in B} T_{\mathfrak{p}}^i$ cuts down this excess, finally leading to a satisfactory prediction of the cumulative turbine thrust.

In summary, the proposed model has a satisfactory performance in this APG condition. It is worth mentioning that the APG condition usually occurs in the high-turbulence leeward region in the atmospheric boundary layer, which is far from the ideal case studied in § 4.2.1. Therefore, although the PG-IMCM model has a poor performance in the ideal APG-CCW-WT case, which is related to the inapplicability of empirical expression for individual velocity deficits, it will not influence its engineering applications in realistic APG conditions similar to the APG-RAMP-WT case, in which it still has a high prediction accuracy.
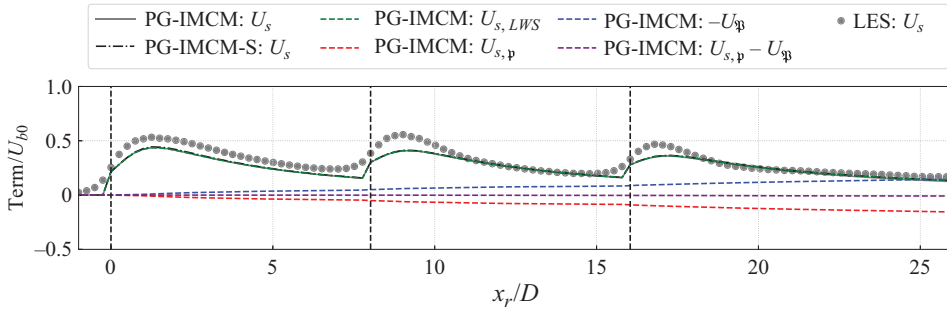
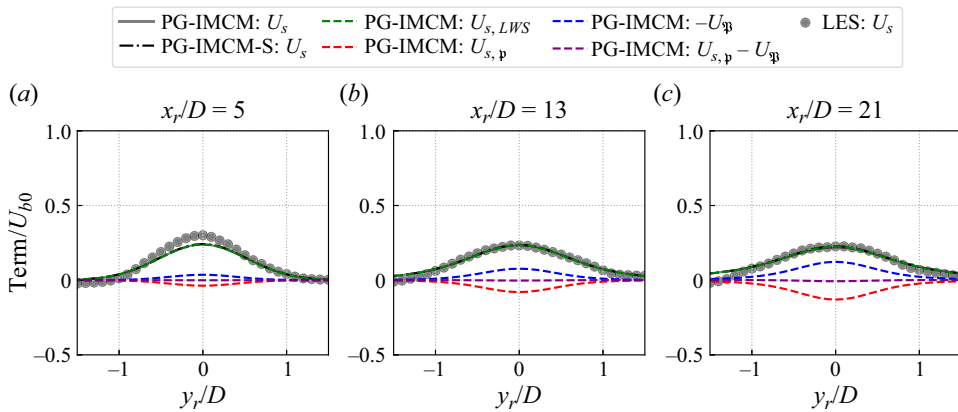Figure 20. Same as figure 8, but for the APG-RAMP-WT case.

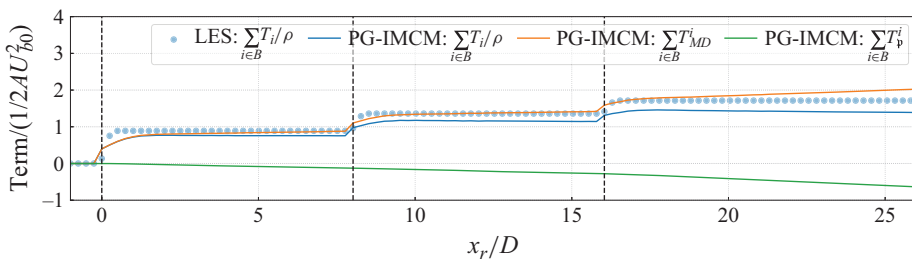Figure 21. Same as figure 9, but for the APG-RAMP-WT case.

Figure 22. Same as figure 10, but for the APG-RAMP-WT case.

5. Comparison with empirical superposition principles

Motivated by the simplified form PG-IMCM-S, which is free of the pressure correction term in the superposition method, it is of great interest to examine the applicability of some empirical superposition principles under pressure gradient. In § 5.1, we extend the empirical superposition methods mentioned in § 1.2 to account for the pressure gradient and compare their predictions with PG-IMCM and LES results in § 5.2.

999 A27-28

WFFAM	Wake superposition model	Wake model	Base flow for WT_i
PG-GL	Global linear	PG wake model	U_b
PG-GS	Global square	PG wake model	U_b
PG-LL	Local linear	PG wake model	u_b^i
PG-LS	Local square	PG wake model	u_b^i
PG-WP	Wind product	PG wake model	u_b^i

Table 4. Classification and details of the proposed empirical WFFAMs under pressure gradient.

5.1. *WFFAMs under pressure gradient based on empirical superposition principles*

Specifically, we can develop five empirical WFFAMs based on the empirical superposition methods (i.e. global linear, global square, local linear, local square and wind product) introduced in § 1.2 and the single-wake model under pressure gradient given in § 2.2. In addition, we have shown that these empirical WFFAMs may have a good performance provided that they can account for the base flow variations based on our derivation, which is also supported by Dar & Porté-Agel (2024). Therefore, their forms have been changed as follows:

$$\text{PG-GL:} \quad U_s(x, y, z) = \sum_i (U_b(x) - u_w^i(x, y, z)), \tag{5.1}$$

$$\text{PG-GS:} \quad U_s(x, y, z) = \sqrt{\sum_i (U_b(x) - u_w^i(x, y, z))^2}, \tag{5.2}$$

$$\text{PG-LL:} \quad U_s(x, y, z) = \sum_i (u_b^i(x) - u_w^i(x, y, z)), \tag{5.3}$$

$$\text{PG-LS:} \quad U_s(x, y, z) = \sqrt{\sum_i (u_b^i(x) - u_w^i(x, y, z))^2}, \tag{5.4}$$

$$\text{PG-WP:} \quad U_s(x, y, z) = U_b(x) - U_b(x) \prod_i \left(\frac{u_w^i(x, y, z)}{u_b^i(x)} \right). \tag{5.5}$$

Compared with their counterparts under the ZPG condition, there are three main differences: (i) U_∞ is replaced by $U_b(x)$; (ii) u_0^i is replaced by $u_b^i(x)$, which is the base flow for WT_i defined in § 2.1.2; (iii) the calculation of $u_w^i(x, y, z)$ will account for the influence of pressure gradient. To be consistent with the different physical meanings between *global* and *linear* under the ZPG condition, the base flow and turbulence intensity used to calculate u_w^i are different. In the *global* superposition methods (i.e. PG-GL and PG-GS), u_w^i is calculated based on $U_b(x)$ and ambient turbulence intensity I_b, whereas u_w^i is calculated based on $u_b^i(x)$ and inflow turbulence intensity I_u^i in the *local* superposition methods (i.e. PG-LL and PG-LS) and PG-WP.

In total, we have developed five empirical WFFAMs under pressure gradient, and their classification and details are given in table 4. They have the same inputs and output as the momentum-conserving model. The step-by-step procedures of these empirical WFFAMs are detailed in Appendix C.
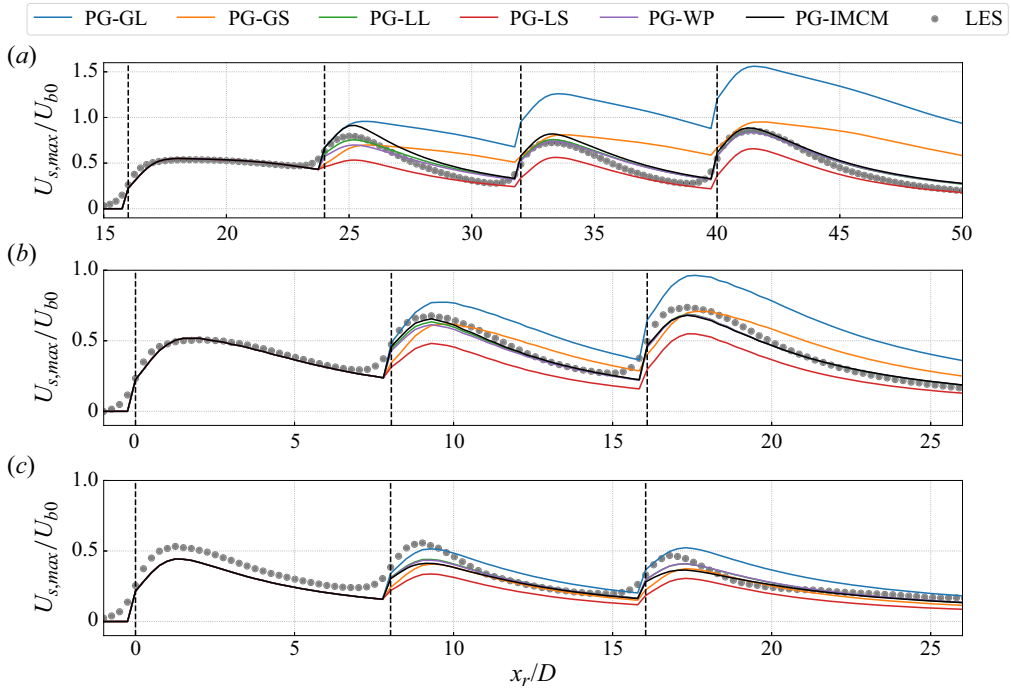
Figure 23. Comparison of $U_{s,max}/U_{b0}$ obtained by different WFFAMs with LES for the cases: (*a*) FPG-CVW-WT, (*b*) FPG-RAMP-WT and (*c*) APG-RAMP-WT. Vertical black dashed lines represent the locations of wind turbines.

5.2. *Validation results*

In this subsection, we inter-compare the prediction results of these five empirical WFFAMs in the FPG-CVW-WT, FPG-RAMP-WT and APG-RAMP-WT cases. Figure 23 shows the comparison of the $U_{s,max}/U_{b0}$ obtained by the empirical WFFAMs and PG-IMCM with LES for the three validation cases. We can see that the prediction of empirical WFFAMs under pressure gradient have many similarities with their counterparts under the ZPG condition. Overall, the PG-GL model will significantly overestimate the wind farm velocity deficit U_s in the merged wake region. This is likely due to the fact that the background velocity, which does not account for the wake effect of upstream wind turbines, is used as the base flow, leading to the overestimation of individual wake velocity deficits. Moreover, when they are summed directly as the PG-GL model, it will overestimate U_s. If they are superimposed as the PG-GS model, it seems that only the largest individual wake velocity deficit will be left, and this may alleviate the overestimation of U_s. However, the PG-GS method still fails to have a satisfactory prediction, especially when the ambient turbulence intensity is low to moderate. If we use the base flow updated by accounting for upstream turbine wakes, the individual velocity deficits may be predicted accurately. However, when they are superimposed as the PG-LS model, it may suffer from the same problems as the PG-GS model, leading to the underestimation of the combined velocity deficit. Overall, the PG-LL model has a satisfactory performance. These findings are consistent with the inter-comparison results under the ZPG condition (Niayifar & Porté-Agel 2016; Zong & Porté-Agel 2020; Bastankhah *et al.* 2021). In addition, the prediction results of the PG-WP model are almost identical to those of the PG-LL model, which is also observed by Lanzilao & Meyers (2022) under the ZPG condition.
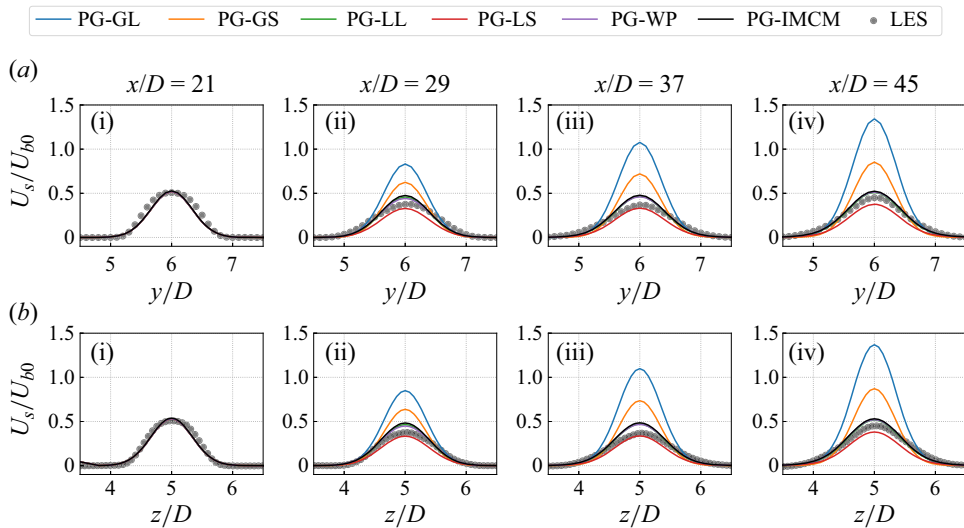
999 A27-30

Figure 24. Comparison of (*a*) the spanwise velocity deficit profiles at hub height and (*b*) vertical velocity deficit profiles at the *x*–*z* rotor symmetry plane obtained by different WFFAMs with LES downstream of each wind turbine for the FPG-CVW-WT case.

Interestingly, the performance of PG-LL and PG-WP is very close to the momentum-conserving method, with only discernable differences in the near-wake region of the merged wake, which has also been observed in Zong & Porté-Agel (2020). This is related to the gradual variation of the mean convection velocity u_c and the sudden change in the combined convection velocity U_c in the near-wake region of downstream turbines, leading to the weights for individual velocity deficits in these regions deviating from 1, which is exactly the weight of the PG-LL model. In contrast, the weight for individual velocity deficits in the PG-IMCM method in the far-wake region of downstream turbines will approach 1, resulting in a nearly collapsed prediction. A direct comparison between PG-WP and PG-IMCM is more intricate, as they have quite different forms. However, we believe that its high prediction accuracy lies in its intrinsic ability to update the base flow for downstream wind turbines, which is supported by Dar & Porté-Agel (2024).

Figures 24–26 further show comparisons of the spanwise and vertical velocity deficit profiles obtained by different WFFAMs against LES results for FPG-CVW-WT, FPG-RAMP-WT and APG-RAMP-WT case, respectively. Overall, the PG-IMCM, PG-LL and PG-WP models have the best performance. As expected, the spanwise and vertical profiles are almost identical in the convex channel case since it is free from the influence of the wall. In contrast, affected by the windward or leeward ramp, the wake velocity deficit has asymmetric characteristics. As a result, the spanwise and vertical wake widths have some differences, especially in the APG-RAMP-WT case. In addition, the wake centre position is slightly shifted downwards with respect to the hub height in the FPG-RAMP-WT case, as shown in figure 12(*a*), whereas the wake centre shifts upwards in the APG-RAMP-WT case, as depicted in figure 19(*a*). These pose significant challenges to accurately predicting the spatial distribution of wake velocity deficit and are difficult to model. Nevertheless, the adoption of the axisymmetric wake model and the same spanwise and vertical wake growth rates in the WFFAMs still have satisfactory performance, as shown in figures 25 and 26(*b*). The difference in the wake width prediction of the APG-RAMP-WT case can be alleviated to some extent by lowering the spanwise wake
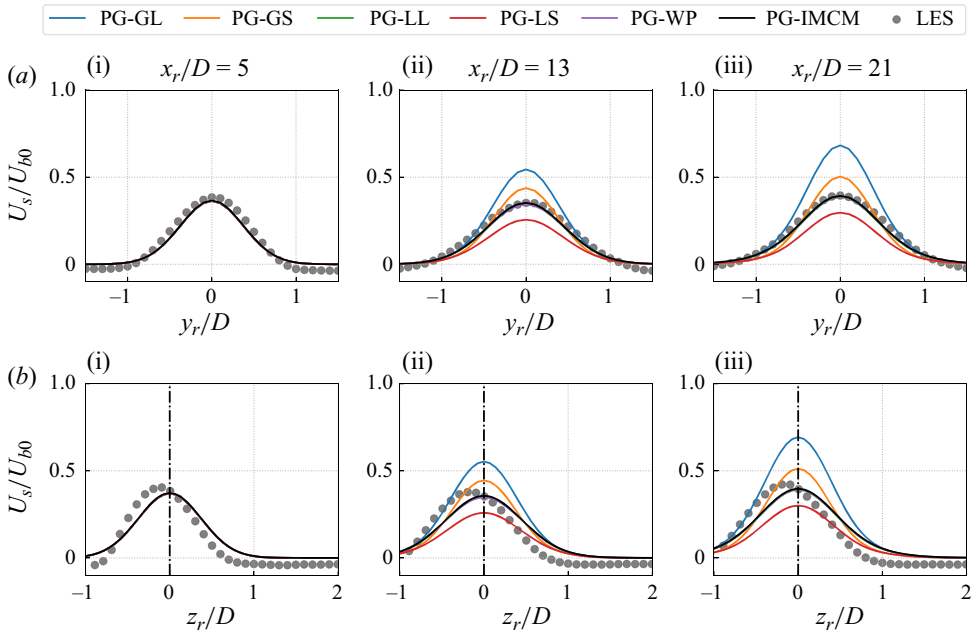
Figure 25. Comparison of (*a*) the spanwise velocity deficit profiles at hub height and (*b*) vertical velocity deficit profiles at the x_r–z_r rotor symmetry plane obtained by different WFFAMs with LES downstream of each wind turbine for the FPG-RAMP-WT case. Black dot-dashed lines represent the hub height.

growth rate slightly and increasing the vertical wake growth rate accordingly to keep the equivalent wake width unchanged. However, developing a general empirical relationship of wake growth rates in different directions is beyond the scope of this study, and it needs to be better understood and addressed in future research.

Overall, the inter-comparison results of the empirical WFFAMs under pressure gradient share many similarities with the inter-comparison results under the ZPG condition. Among the five considered empirical models, the PG-LL and PG-WP models have a satisfactory and consistent performance with the PG-IMCM model in all validation cases, especially in realistic ramp cases. The secret behind their good performance can be attributed to the ability to properly update the base flow for the downstream wind turbines as well as reasonable superposition principles.

6. Conclusions

Pressure gradient over topography will significantly affect the wind-farm flow. To date, the wake superposition method and WFFAMs that account for its effect are unexplored, which significantly limits engineering applications such as wind farm wake loss evaluation and micro-site selection over complex terrain. To bridge this gap, we have theoretically derived an implicit momentum-conserving superposition method under pressure gradient (PG-IMCM). Based on the physical insights gained in the model derivation, we have further investigated the empirical superposition methods. In addition, we have systematically validated their performance based on LESs.

The PG-IMCM method has been derived based on the simplified integral RANS equation, which states that the total momentum deficit is equal to the sum of wind-turbine thrusts and the integral of pressure correction $\mathfrak{P}$ induced by the wind-farm velocity deficit
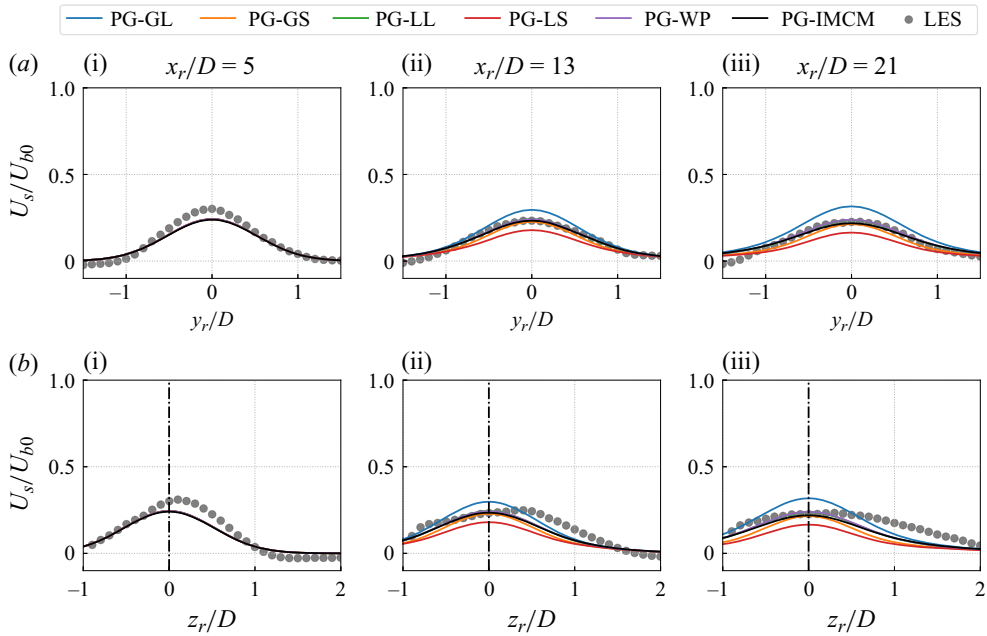
Figure 26. Same as figure 25, but for the APG-RAMP-WT case.

U_s. For an arbitrary wind turbine under pressure gradient, its thrust can be decomposed into the momentum deficit and the integral of pressure correction $\mathfrak{p}$ induced by its own velocity deficit u_s. The momentum deficit for the single turbine wake and the total momentum deficit under pressure gradient can be linearised by the mean convection velocity u_c and the combined convection velocity U_c, respectively, which are introduced by Zong & Porté-Agel (2020). After linearisation, we can see that the wind-farm velocity deficit U_s consists of the linear-weighted sum of individual wake velocity deficits, the sum of the pressure correction terms induced by individual wake velocity deficit divided by U_c, and pressure correction term induced by wind-farm velocity deficit divided by U_c.

Based on an order-of-magnitude and sensitivity study representing typical wind farm operational conditions, we can verify that the sum of the last two terms has a relatively small value, only about 0.4 % of the first term, and thus can be neglected, resulting in a simplified form PG-IMCM-S, which only includes the linear-weighted sum of individual wake velocity deficits. It is noteworthy that PG-IMCM-S has the same form as its counterpart under the ZPG condition, but with the single-wake quantities redefined based on the wake model under pressure gradient. Individual wake velocity deficit u_s is modelled as the asymptotic solution of the stand-alone wake model under pressure gradient, and the mean convection velocity u_c is generalised to account for the influence of pressure gradient on the single-turbine wake evolution.

The proposed PG-IMCM model and its simplified form have been validated based on the ideal convex/concave channel cases and the realistic ramp cases simulated by LES with the wall-modelled IBM. The results show that our proposed model can accurately represent wind turbine thrust, validating some assumptions used to derive the model. PG-IMCM and its simplified form have virtually identical prediction results, and they can predict the maximum velocity deficit and spanwise velocity deficit profiles at hub height very well, except for the ideal concave channel. The overestimation of wind-farm velocity deficit

for the ideal concave channel may be attributed to the inapplicability of empirical wake growth rate relation rather than the proposed superposition method. The above finding points out one limitation of the proposed method, that is, its accuracy is quite sensitive to the individual wake velocity deficit modelling, especially the wake growth rate, which is still an ongoing research topic. Nevertheless, the empirical relations used in our study can provide good prediction capability in the realistic ramp cases, which is of great significance to engineering applications.

Last but not least, we have developed five empirical superposition methods accounting for pressure gradient (i.e. PG-GL, PG-GS, PG-LL, PG-LS and PG-WP) based on the global linear, global square, local linear, local square and wind product superposition principles, respectively, which are well-defined under the ZPG condition. Their differences mainly lie in the adoption of the spatial-varying base flow and the calculation of individual wake velocity deficit. Further inter-comparison results have shown that PG-GL and PG-GS significantly overestimate the velocity deficit in the merged wake region, whereas PG-LS underestimates this quantity. PG-LL and PG-WP have the best performance, and they nearly collapse with the momentum-conserving method, with only discernable differences in the near-wake region of the merged wake. The high accuracy of these two empirical methods lies in their ability to properly update the base flow for downstream wind turbines and their superposition principles.

In summary, the PG-IMCM method and its simplified version perform relatively well in various validation cases, provided that the individual wake velocity deficits can be modelled accurately. They can be used to evaluate the influence of pressure gradient on wind-farm flows over complex terrain. In addition, PG-LL and PG-WP are two attractive empirical superposition methods, as they have comparable prediction accuracy but much lower computational cost in comparison with the momentum-conserving method.

Future research will focus on the validation of the proposed method under the partial-wake or deep-array condition, which is generally viewed as more challenging for the wake superposition method.

Author ORCIDs.
- Bowen Du https://orcid.org/0000-0003-4295-2002;
- Mingwei Ge https://orcid.org/0000-0001-7070-7122.

Appendix A. Step-by-step procedure of the momentum-conserving WFFAM

From the perspective of code implementation, the PG-IMCM and PG-IMCM-S have a recursive cycle to update the base flow for downstream turbines one by one. Moreover, we employ an iteration method to ensure the convergence of the combined convection velocity U_c in each recursive step. The step-by-step procedure is as follows.

(1) Calculate the single-turbine wake quantities of WT_i ($1 \leq i \leq N$) under ZPG.

    (1.1) Added turbulence intensity model of Ishihara & Qian (2018) $\rightarrow \delta I_u^{j \rightarrow i}$.

(1.2) Maximum added turbulence superposition model of Niayifar & Porté-Agel (2016) $\rightarrow I_u^i$.

(1.3) Wake growth rate model $\rightarrow k_w^i$.

(1.4) Near-wake length model $\rightarrow x_{th}^i$.

(1.5) Quasi-linear growth model for wake width $\rightarrow \sigma_0^i(x)$.

(1.6) Normalised maximum velocity deficit model under the ZPG condition $\rightarrow C_0^i(x)$.

(2) Assume that there are n wind turbines with the initial value of $n = 1$ and calculate the wind-farm velocity deficit U_s^n for n wind turbines.

  (2.1) Calculate the stand-alone turbine wake quantities of WT_i ($1 \leq i \leq n$) under pressure gradient.

    (2.1.1) Normalised maximum velocity deficit under pressure gradient $\rightarrow C^i(x) = C_0^i(x)[u_b^i(x_i)/u_b^i(x)]^{5/3}$.

    (2.1.2) Mean convection velocity model under pressure gradient $\rightarrow u_c^i = u_b^i(x)(1 - C^i(x)/2)$.

    (2.1.3) Wake width under pressure gradient $\rightarrow \sigma^i(x) = \sigma_0^i(x)[u_b^i(x_i)/u_b^i(x)]^{2/3}$.

    (2.1.4) Wake velocity deficit under pressure gradient $\rightarrow u_s^i(x, y, z) = u_b^i(x)C^i(x) \exp(-[(y - y_i)^2 + (z - z_i)^2]/2(\sigma^i)^2)$.

  (2.2) Set up the initial $U_c^0(x)$ for the iteration based on the maximum value of $u_c^i(x)$, i.e. $U_c^0(x) = \max_i[u_c^i(x)]$.

  (2.3) Calculate the wind farm velocity deficit based on PG-IMCM or its simplified form.

   (i) PG-IMCM:

$$U_s^n(x, y, z) = \sum_{i=1}^n \frac{u_c^i(x)}{U_c^0(x)} u_s^i(x, y, z) + \frac{\sum_{i=1}^n \mathfrak{p}^i - \mathfrak{P}}{U_c^0(x)}. \tag{A1}$$

   (ii) PG-IMCM-S:

$$U_s^n(x, y, z) \approx \sum_{i=1}^n \frac{u_c^i(x)}{U_c^0(x)} u_s^i(x, y, z). \tag{A2}$$

  (2.4) Calculate the combined convection velocity for wind-farm flows according to (2.18) $\rightarrow U_c^*(x)$.

  (2.5) Determine whether the iteration has reached convergence. The iteration criterion is

$$\frac{\overline{|U_c^*(x) - U_c^0(x)|}}{U_c^*(x)} < 0.001. \tag{A3}$$

    If (A3) is met, the iteration stops; if not, $U_c^0(x) = U_c^*(x)$ and repeat (2.3)–(2.5) until the iteration criterion is satisfied.

(3) Update the base flow u_b^{n+1} for WT_{n+1} based on the definition $u_b^{n+1}(x) = U_b(x) - (1/N_q) \sum_{q=1}^{N_q} U_s^n(x, y_{n+1,q}, z_{n+1,q})$.

(4) Compare n and N. If $n = N$, output U_s^n; otherwise, $n = n + 1$ and repeat steps (2)–(4) until $n = N$.

Appendix B. Comments on the applicability of the asymptotic solution and near-wake width model

B.1. *Comparison of the ODE and its asymptotic solution for wind-turbine wakes under pressure gradient*

Strictly speaking, the normalised maximum velocity deficit $C(x)$ under pressure gradient can be solved by an ODE derived by Shamsoddin & Porté-Agel (2018a), as follows:

$$\frac{\mathrm{d}C(x)}{\mathrm{d}x} = \frac{-1}{\left(\frac{U_b^4}{\lambda_0^2}\right)(3C^2 - 2C^3)}\left[\frac{1}{4}\frac{\mathrm{d}U_b^4}{\mathrm{d}x}\frac{C^3}{\lambda_0^2} + \left(C^3 - \frac{C^4}{2}\right)\frac{\mathrm{d}}{\mathrm{d}x}\left(\frac{U_b^4}{\lambda_0^2}\right)\right], \quad (B1)$$

which can be integrated from upstream to downstream provided that the parameters $U_b(x)$, $\lambda_0(x)$ and a boundary condition $C(x_{bc}) = C_0(x_{bc})$ are given. When C is obtained, wake width σ under pressure gradient can be calculated by $\sigma = (U_b/\lambda_0)C$. In this appendix, we compare the asymptotic solution used in our study with the ODE solution. The base flow is given as

$$U_b(x) = U_{b0}[1 + c(x - x_t)/D], \quad (B2)$$

where U_{b0} is the freestream incoming speed at the streamwise location of the wind turbine, c is defined as the normalised speed-up ratio and $x_t = 2D$ is the streamwise location of the wind turbine.

To begin with, we present a case study to showcase some calculation details about these two solutions. The normalised speed-up ratio c is set to -0.02 and 0.02 to represent the APG and FPG conditions, respectively. The ambient turbulence intensity I_b is 0.06, and the thrust coefficient C_T is 0.8. The base flow, C_0, σ_0 and λ_0 are shown in figure 27. Here $C(x)$ and $\sigma(x)$ solved by the ODE and its asymptotic solution are shown in figure 28. It can be seen that the ODE solution and its asymptotic solution are nearly collapsed, provided that the ODE is integrated from the end of the thrust coefficient correction, i.e. $x_{bc} = x_t + 2D$, rather than the location of the wind turbine.

Furthermore, we consider the performance of the asymptotic solution under different atmospheric conditions corresponding to the typical operational condition of the wind turbine, as listed in table 5. We can define error metrics for $C(x)$ and $\sigma(x)$ to quantify the error using the asymptotic solution with respect to the ODE solution. For each considered atmospheric state, we can calculate the mean absolute percentage error for $C(x)$ and $\sigma(x)$ as follows:

$$\mathrm{MAPE}_q = \frac{100\%}{12D}\int_{x_{bc}}^{x_{bc}+12D}\frac{|q_{ODE}(x) - q_{ASY}(x)|}{q_{ODE}(x)}\,\mathrm{d}x \quad (q \text{ is } C \text{ or } \sigma). \quad (B3)$$

Finally, we can obtain the case-averaged $\overline{\mathrm{MAPE}}_{C,\sigma}$. Based on the atmospheric states considered in table 5, $\overline{\mathrm{MAPE}}_{C,\sigma} = 4.3\%$, indicating that using the asymptotic solution in the WFFAMs will only have negligible errors compared with the ODE. Given its comparable accuracy, low computational cost and ease of use in comparison with the ODE, we use the asymptotic solution as the single-wake model throughout the paper.
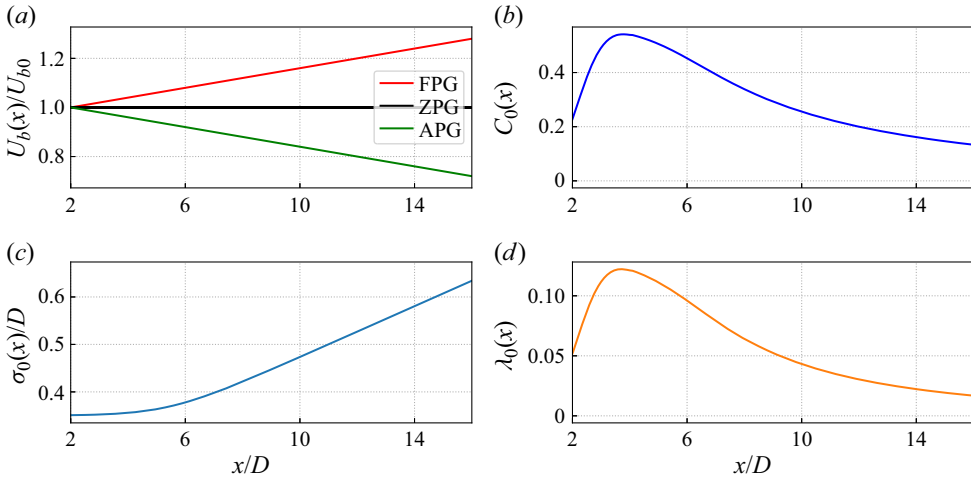
Figure 27. Inputs for the calculation of the ODE and its asymptotic solution: (*a*) the base flow variation, (*b*) the maximum normalised velocity deficit under the ZPG condition, (*c*) wake width under the ZPG condition and (*d*) pressure gradient invariant ratio.
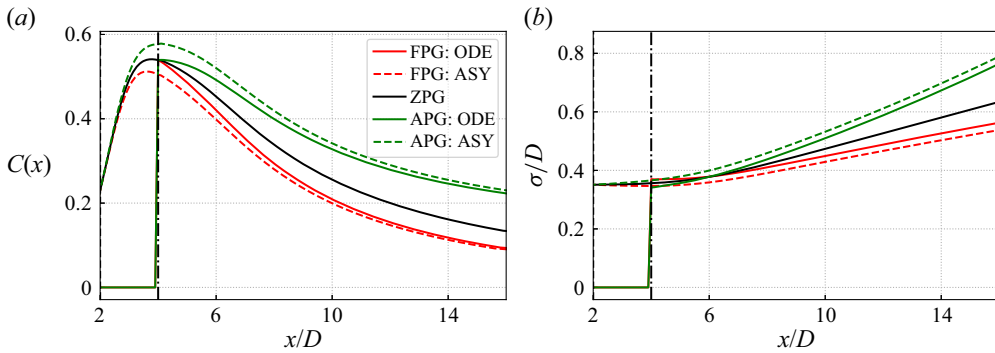

Figure 28. Comparison of the results from the ODE with its asymptotic solution: (*a*) the normalised maximum velocity deficit $C(x)$ and (*b*) wake width $\sigma(x)$. The dash-dotted line represents x_{bc}.

B.2. *Comparison of the near-wake width models under pressure gradient*

In the modelling of the near-wake width x_{th}, we resort to the analytical model proposed by Bastankhah & Porté-Agel (2016):

$$x_{th}^{ZPG} = \frac{(1 + \sqrt{1 - C_T})\sigma_0^{nw}}{2\alpha I_u + \beta(1 - \sqrt{1 - C_T})}, \tag{B4}$$

where $\sigma_0^{nw} = 1/2\sqrt{2}D$ is the near-wake width under ZPG and $\alpha = 0.9$ and $\beta = 0.077$ are the fitted parameters based on field measurements (Carbajo Fuertes *et al.* 2018). Recently, Dar *et al.* (2023) extends the above expression to account for the influence of pressure gradient, and the near-wake length x_{th}^{PG} under pressure gradient has an implicit relationship

Description	Values
Wind-turbine configuration:	
Turbine thrust coefficient	$C_T = 0.8$
Atmospheric state:	
Normalised speed-up ratio	$c = -0.03, -0.02, \ldots, 0.03$
Ambient turbulence intensity	$I_b = 0.03, 0.05, \ldots, 0.15$

Table 5. Case set-up for the sensitivity study of the asymptotic solution and near-wake length model for single-turbine wake modelling.
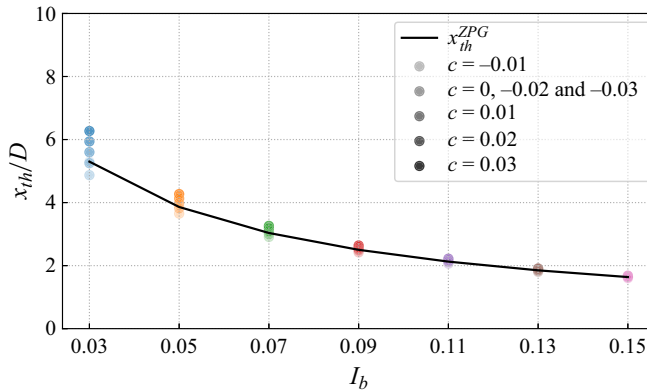

Figure 29. Comparison of the results from (B4) and (B5).

with the near-wake width σ_{nw}, as follows:

$$\sigma_0^{nw} = (2\alpha I_u + \beta) \int_0^{x_{th}^{PG}} \frac{1}{1 + \sqrt{1 - \dfrac{U_{b0}^2 C_T}{(\gamma x + U_{b0})^2}}} \, \mathrm{d}x$$

$$- \beta \int_0^{x_{th}^{PG}} \frac{1}{1 + 1/\sqrt{1 - \dfrac{U_{b0}^2 C_T}{(\gamma x + U_{b0})^2}}} \, \mathrm{d}x, \tag{B5}$$

where $\gamma = cU_{b0}/D$ is the flow speed-up factor. When $\gamma = 0$, (B5) is essentially the same as (B4) under the ZPG condition. Unlike (B4), x_{th}^{PG} in (B5) must be calculated numerically by scientific languages, such as Matlab and Python. It should be noted that (B5) can only be solved when $\gamma x_{th}^{PG} > U_{b0}(\sqrt{C_T} - 1)$, which is likely to be avoided under APG condition. Here, we will compare the near-wake width x_{th}^{ZPG} and x_{th}^{PG} calculated by (B4) and (B5), respectively. The thrust coefficient C_T is set to 0.8, while ambient turbulence intensity and the base flow are varied according to table 5. If (B5) cannot be solved, we will set $x_{th}^{PG} = x_{th}^{ZPG}$ directly, which is the case for $c = -0.03$ and -0.02. The results are shown in figure 29.

It can be seen that the near-wake length is more sensitive to the variation of I_b than c, which can be captured by (B4) very well. The influence of pressure gradient

999 A27-38

on the near-wake length significantly depends on the ambient turbulence intensity. The smaller the I_b, the more obvious influence of c. Similar to (B3), we can also define the case-averaged mean absolute percentage error for x_{th} as follows:

$$\overline{\text{MAPE}}_{x_{th}} = \frac{100\,\%}{N_{I_b} N_c} \sum_{I_b} \sum_{c} \frac{|x_{th}^{ZPG}(I_b) - x_{th}^{PG}(I_b, c)|}{x_{th}^{ZPG}(I_b)}, \tag{B6}$$

where $N_{I_b} = 7$ and $N_c = 7$ are the number of different I_b and c cases, respectively. Based on the atmospheric states considered in table 5, $\overline{\text{MAPE}}_{x_{th}} = 1.3\,\%$. In view of its comparable accuracy, low computational cost and robustness with respect to its counterpart under pressure gradient, we use (B4) as the near-wake length model in the study.

Appendix C. WFFAMs based on the empirical superposition principles

The proposed five empirical WFFAMs have differences in the definition of the base flow, the calculation of individual velocity deficits and the superposition principle. According to these differences, the five empirical WFFAMs can be classified into three categories.

C.1. *PG-GL and PG-GS WFFAMs*

These two models use the base flow $U_b(x)$ as the background velocity to calculate individual velocity deficits, and their main difference is how to merge the individual velocity deficits. The code implementation of these two methods is very similar, so they are gathered together as follows.

(1) Calculate the single-turbine wake quantities of WT_i ($1 \leq i \leq N$) under ZPG. Except for $I_u^i = I_b$, other details are the same as step (1) in Appendix A and thus not repeated here.
(2) Normalised maximum velocity deficit of WT_i under pressure gradient $\rightarrow C^i(x) = C_0^i(x)[U_b(x_i)/U_b(x)]^{5/3}$.
(3) Wake width of WT_i under pressure gradient $\rightarrow \sigma^i(x) = \sigma_0^i(x)[U_b(x_i)/U_b(x)]^{2/3}$.
(4) Wake velocity deficit of WT_i under pressure gradient based on $U_b(x) \rightarrow u_s^i(x, y, z) = U_b(x)C^i(x)\exp(-[(y - y_i)^2 + (z - z_i)^2]/2(\sigma^i)^2)$.
(5) Calculate the wind-farm velocity deficit $U_s(x, y, z)$ using the *linear/square* superposition principles:
  (i) PG-GL: $U_s(x, y, z) = \sum_{i=1}^N u_s^i(x, y, z)$;
  (ii) PG-GS: $U_s(x, y, z) = \sqrt{\sum_{i=1}^N u_s^i(x, y, z)^2}$.

C.2. *PG-LL and PG-LS WFFAMs*

The main difference between these two *local* WFFAMs from the *global* WFFAMs is the calculation of base flow u_b^i for downstream turbines, which should be determined by a recursive procedure. By definition, $u_b^1(x) = U_b(x)$. The code implementation of these two methods is very similar, with minor differences in the superposition principle, so they are presented together as follows.

(1) Calculate the single turbine wake quantities of WT_i ($1 \leq i \leq N$) under ZPG. The detail is the same as step (1) in Appendix A and thus not repeated here.

(2) Assume that there are n wind turbines with the initial value $n = 1$, and calculate the wind-farm velocity deficit U_s^n for n wind turbines.

    (2.1) Normalised maximum velocity deficit of WT_i $(1 \le i \le n)$ under pressure gradient $\rightarrow C^i(x) = C_0^i(x)[u_b^i(x_i)/u_b^i(x)]^{5/3}$.

    (2.2) Wake width of WT_i $(1 \le i \le n)$ under pressure gradient $\rightarrow \sigma^i(x) = \sigma_0^i(x)[u_b^i(x_i)/u_b^i(x)]^{2/3}$.

    (2.3) Wake velocity deficit of WT_i $(1 \le i \le n)$ under pressure gradient based on $u_b^i(x) \rightarrow u_s^i(x, y, z) = u_b^i(x)C^i(x) \exp(-[(y - y_i)^2 + (z - z_i)^2]/2(\sigma^i)^2)$.

    (2.4) Calculate the wind-farm velocity deficit $U_s^n(x, y, z)$ using the *linear/square* superposition principles:

       (i) PG-LL: $U_s^n(x, y, z) = \sum_{i=1}^n u_s^i(x, y, z)$;

       (ii) PG-LS: $U_s^n(x, y, z) = \sqrt{\sum_{i=1}^n u_s^i(x, y, z)^2}$.

(3) Update the base flow u_b^{n+1} for WT_{n+1} based on the definition $u_b^{n+1}(x) = U_b(x) - (1/N_q) \sum_{q=1}^{N_q} U_s^n(x, y_{n+1,q}, z_{n+1,q})$.

(4) Compare n and N. If $n = N$, output U_s^n; otherwise, $n = n + 1$ and repeat steps (2)–(4).

C.3. *PG-WP WFFAM*

The essence of the wind product method is different from the above superposition methods, in which the wind-farm flow velocity deficit U_s is determined by the superposition of individual wake velocity deficits. In the wind product method, U_s is determined by subtracting the wind-farm flow U_w from the base flow $U_b(x)$, in which U_w is calculated by a product between the base flow and the normalised individual wake velocity. Therefore, its code implementation has some differences from other empirical methods, and the details are presented in the following.

(1) Calculate the single-turbine wake quantities of WT_i $(1 \le i \le N)$ under ZPG. The detail is the same as step (1) in Appendix A and thus not repeated here.

(2) Assume that there are n wind turbines with the initial value $n = 1$, and calculate the wind-farm velocity deficit U_s^n for n wind turbines.

    (2.1) Normalised maximum velocity deficit of WT_i $(1 \le i \le n)$ under pressure gradient $\rightarrow C^i(x) = C_0^i(x)[u_b^i(x_i)/u_b^i(x)]^{5/3}$.

    (2.2) Wake width of WT_i $(1 \le i \le n)$ under pressure gradient $\rightarrow \sigma^i(x) = \sigma_0^i(x)[u_b^i(x_i)/u_b^i(x)]^{2/3}$.

    (2.3) Normalised wake velocity deficit of WT_i $(1 \le i \le n)$ under pressure gradient $\rightarrow u_s^i(x, y, z)/u_b^i(x) = C^i(x) \exp(-[(y - y_i)^2 + (z - z_i)^2]/2(\sigma^i)^2)$.

    (2.4) Calculate the wind-farm velocity deficit $U_s^n(x, y, z) \rightarrow U_s^n(x, y, z) = U_b(x) - U_b(x) \prod_{i=1}^n [1 - u_s^i(x, y, z)/u_b^i(x)]$.

(3) Update the background velocity u_b^{n+1} for WT_{n+1} based on the definition $u_b^{n+1}(x) = U_b(x) - (1/N_q) \sum_{q=1}^{N_q} U_s^n(x, y_{n+1,q}, z_{n+1,q})$.

(4) Compare n and N. If $n = N$, output U_s^n; otherwise, $n = n + 1$ and repeat steps (2)–(4).

999 A27-40

REFERENCES

ALLAERTS, D. & MEYERS, J. 2019 Sensitivity and feedback of wind-farm-induced gravity waves. *J. Fluid Mech.* **862**, 990–1028.

ARCHER, C.L., VASEL-BE-HAGH, A., YAN, C., WU, S., PAN, Y., BRODIE, J.F. & MAGUIRE, A.E. 2018 Review and evaluation of wake loss models for wind energy applications. *Appl. Energy* **226**, 1187–1207.

BASTANKHAH, M. & PORTÉ-AGEL, F. 2014 A new analytical model for wind-turbine wakes. *Renew. Energy* **70**, 116–123.

BASTANKHAH, M. & PORTÉ-AGEL, F. 2016 Experimental and theoretical study of wind turbine wakes in yawed conditions. *J. Fluid Mech.* **806**, 506–541.

BASTANKHAH, M., WELCH, B.L., MARTÍNEZ-TOSSAS, L.A., KING, J. & FLEMING, P. 2021 Analytical solution for the cumulative wake of wind turbines in wind farms. *J. Fluid Mech.* **911**, A53.

BAY, C.J., FLEMING, P., DOEKEMEIJER, B., KING, J., CHURCHFIELD, M. & MUDAFORT, R. 2023 Addressing deep array effects and impacts to wake steering with the cumulative-curl wake model. *Wind Energy Sci.* **8** (3), 401–419.

BLONDEL, F. 2023 Brief communication: a momentum-conserving superposition method applied to the super-Gaussian wind turbine wake model. *Wind Energy Sci.* **8** (2), 141–147.

BOU-ZEID, E., MENEVEAU, C. & PARLANGE, M. 2005 A scale-dependent Lagrangian dynamic model for large eddy simulation of complex turbulent flows. *Phys. Fluids* **17** (2), 025105.

BROGNA, R., FENG, J., SØRENSEN, J.N., SHEN, W.Z. & PORTÉ-AGEL, F. 2020 A new wake model and comparison of eight algorithms for layout optimization of wind farms in complex terrain. *Appl. Energy* **259**, 114189.

CARBAJO FUERTES, F., MARKFORT, C.D. & PORTÉ-AGEL, F. 2018 Wind turbine wake characterization with nacelle-mounted wind lidars for analytical wake model validation. *Remote Sens.* **10** (5), 668.

CHESTER, S., MENEVEAU, C. & PARLANGE, M.B. 2007 Modeling turbulent flow over fractal trees with renormalized numerical simulation. *J. Comput. Phys.* **225** (1), 427–448.

CRESPO, A., HERNANDEZ, J. & FRANDSEN, S. 1999 Survey of modelling methods for wind turbine wakes and wind farms. *Wind Energy* **2** (1), 1–24.

DAR, A.S., GERTLER, A.S. & PORTÉ-AGEL, F. 2023 An experimental and analytical study of wind turbine wakes under pressure gradient. *Phys. Fluids* **35** (4), 045140.

DAR, A.S. & PORTÉ-AGEL, F. 2022 An analytical model for wind turbine wakes under pressure gradient. *Energies* **15** (15), 5345.

DAR, A.S. & PORTÉ-AGEL, F. 2024 Wind turbine wake superposition under pressure gradient. *Phys. Fluids* **36** (1), 015145.

DU, B., GE, M. & LIU, Y. 2022 A physical wind-turbine wake growth model under different stratified atmospheric conditions. *Wind Energy* **25** (10), 1812–1836.

DU, B., GE, M., ZENG, C., CUI, G. & LIU, Y. 2021 Influence of atmospheric stability on wind-turbine wakes with a certain hub-height turbulence intensity. *Phys. Fluids* **33** (5), 055111.

FAN, X., GE, M., TAN, W. & LI, Q. 2021 Impacts of coexisting buildings and trees on the performance of rooftop wind turbines: an idealized numerical study. *Renew. Energy* **177**, 164–180.

FARRELL, A., KING, J., DRAXL, C., MUDAFORT, R., HAMILTON, N., BAY, C.J., FLEMING, P. & SIMLEY, E. 2021 Design and analysis of a wake model for spatially heterogeneous flow. *Wind Energy Sci.* **6** (3), 737–758.

FENG, J., SHEN, W.Z. & LI, Y. 2018 An optimization framework for wind farm design in complex terrain. *Appl. Sci.* **8** (11), 2053.

FINNIGAN, J., AYOTTE, K., HARMAN, I., KATUL, G., OLDROYD, H., PATTON, E., POGGI, D., ROSS, A. & TAYLOR, P. 2020 Boundary-layer flow over complex topography. *Boundary-Layer Meteorol.* **177**, 247–313.

GAMBUZZA, S. & GANAPATHISUBRAMANI, B. 2023 The influence of free stream turbulence on the development of a wind turbine wake. *J. Fluid Mech.* **963**, A19.

GE, M., YANG, H., ZHANG, H. & ZUO, Y. 2021 A prediction model for vertical turbulence momentum flux above infinite wind farms. *Phys. Fluids* **33** (5), 055108.

GE, M., ZHANG, S., MENG, H. & MA, H. 2020 Study on interaction between the wind-turbine wake and the urban district model by large eddy simulation. *Renew. Energy* **157**, 941–950.

GUPTA, V. & WAN, M. 2019 Low-order modelling of wake meandering behind turbines. *J. Fluid Mech.* **877**, 534–560.

HUNT, J.C.R., LEIBOVICH, S. & RICHARDS, K.J. 1988 Turbulent shear flows over low hills. *Q. J. R. Meteorol. Soc.* **114** (484), 1435–1470.

ISHIHARA, T. & QIAN, G.-W. 2018 A new Gaussian-based analytical wake model for wind turbines considering ambient turbulence intensities and thrust coefficient effects. *J. Wind Engng Ind. Aerodyn.* **177**, 275–292.

KATIC, I., HØJSTRUP, J. & JENSEN, N.O. 1986 A simple model for cluster efficiency. In *European Wind Energy Association Conference and Exhibition*, vol. 1, pp. 407–410. A. Raguzzi Rome.

LANZILAO, L. & MEYERS, J. 2022 A new wake-merging method for wind-farm power prediction in the presence of heterogeneous background velocity fields. *Wind Energy* **25** (2), 237–259.

LI, L., WANG, B., GE, M., HUANG, Z., LI, X. & LIU, Y. 2023 A novel superposition method for streamwise turbulence intensity of wind-turbine wakes. *Energy* **276**, 127491.

LI, Z., DONG, G. & YANG, X. 2022 Onset of wake meandering for a floating offshore wind turbine under side-to-side motion. *J. Fluid Mech.* **934**, A29.

LIN, M. & PORTÉ-AGEL, F. 2022 Large-eddy simulation of a wind-turbine array subjected to active yaw control. *Wind Energy Sci.* **7** (6), 2215–2230.

LISSAMAN, P.B.S. 1979 Energy effectiveness of arbitrary arrays of wind turbines. *J. Energy* **3** (6), 323–328.

LIU, L. & STEVENS, R.J.A.M. 2020*a* Effects of two-dimensional steep hills on the performance of wind turbines and wind farms. *Boundary-Layer Meteorol.* **176**, 251–269.

LIU, L. & STEVENS, R.J.A.M. 2020*b* Wall modeled immersed boundary method for high Reynolds number flow over complex terrain. *Comput. Fluids* **208**, 104604.

LIU, Z., LU, S. & ISHIHARA, T. 2021 Large eddy simulations of wind turbine wakes in typical complex topographies. *Wind Energy* **24** (8), 857–886.

MA, H., GE, M., WU, G., DU, B. & LIU, Y. 2021 Formulas of the optimized yaw angles for cooperative control of wind farms with aligned turbines to maximize the power production. *Appl. Energy* **303**, 117691.

MAO, X. & SØRENSEN, J.N. 2018 Far-wake meandering induced by atmospheric eddies in flow past a wind turbine. *J. Fluid Mech.* **846**, 190–209.

MESSMER, T., HÖLLING, M. & PEINKE, J. 2024 Enhanced recovery caused by nonlinear dynamics in the wake of a floating offshore wind turbine. *J. Fluid Mech.* **984**, A66.

NIAYIFAR, A. & PORTÉ-AGEL, F. 2016 Analytical modeling of wind farms: a new approach for power prediction. *Energies* **9** (9), 741.

PORTÉ-AGEL, F., BASTANKHAH, M. & SHAMSODDIN, S. 2020 Wind-turbine and wind-farm flows: a review. *Boundary-Layer Meteorol.* **174** (1), 1–59.

SHAMSODDIN, S. & PORTÉ-AGEL, F. 2017 Turbulent planar wakes under pressure gradient conditions. *J. Fluid Mech.* **830**, R4.

SHAMSODDIN, S. & PORTÉ-AGEL, F. 2018*a* A model for the effect of pressure gradient on turbulent axisymmetric wakes. *J. Fluid Mech.* **837**, R3.

SHAMSODDIN, S. & PORTÉ-AGEL, F. 2018*b* Wind turbine wakes over hills. *J. Fluid Mech.* **855**, 671–702.

SHAPIRO, C.R., GAYME, D.F. & MENEVEAU, C. 2018 Modelling yawed wind turbine wakes: a lifting line approach. *J. Fluid Mech.* **841**, R1.

SHAPIRO, C.R., GAYME, D.F. & MENEVEAU, C. 2019 Filtered actuator disks: theory and application to wind turbine models in large eddy simulation. *Wind Energy* **22** (10), 1414–1420.

STEVENS, R.J.A.M., GRAHAM, J. & MENEVEAU, C. 2014 A concurrent precursor inflow method for large eddy simulations and applications to finite length wind farms. *Renew. Energy* **68**, 46–50.

STEVENS, R.J.A.M., MARTÍNEZ-TOSSAS, L.A. & MENEVEAU, C. 2018 Comparison of wind farm large eddy simulations using actuator disk and actuator line models with wind tunnel experiments. *Renew. Energy* **116**, 470–478.

STEVENS, R.J.A.M. & MENEVEAU, C. 2017 Flow structure and turbulence in wind farms. *Annu. Rev. Fluid Mech.* **49**, 311–339.

SUN, H., YANG, H. & GAO, X. 2023 Investigation into wind turbine wake effect on complex terrain. *Energy* **269**, 126767.

TENG, J. & MARKFORT, C.D. 2020 A calibration procedure for an analytical wake model using wind farm operational data. *Energies* **13** (14), 3537.

THOMAS, F.O. & LIU, X. 2004 An experimental investigation of symmetric and asymmetric turbulent wake development in pressure gradient. *Phys. Fluids* **16** (5), 1725–1745.

VAHIDI, D. & PORTÉ-AGEL, F. 2022 A physics-based model for wind turbine wake expansion in the atmospheric boundary layer. *J. Fluid Mech.* **943**, A49.

VAN KUIK, G.A.M., *et al.* 2016 Long-term research challenges in wind energy – a research agenda by the European academy of wind energy. *Wind Energy Sci.* **1** (1), 1–39.

VOUTSINAS, S., RADOS, K. & ZERVOS, A. 1990 On the analysis of wake effects in wind parks. *Wind Engng* **14** (4), 204–219.

WANG, D., FENG, D., PENG, H., MAO, F., DORANEHGARD, M.H., GUPTA, V., LI, L.K.B. & WAN, M. 2023 Implications of steep hilly terrain for modeling wind-turbine wakes. *J. Clean Prod.* **398**, 136614.

WU, Y.-T. & PORTÉ-AGEL, F. 2011 Large-eddy simulation of wind-turbine wakes: evaluation of turbine parametrisations. *Boundary-Layer Meteorol.* **138**, 345–366.

YANG, H., GE, M., ABKAR, M. & YANG, X.I.A. 2022 Large-eddy simulation study of wind turbine array above swell sea. *Energy* **256**, 124674.

ZHANG, H., GE, M., LIU, Y. & YANG, X.I.A. 2021*a* A new coupled model for the equivalent roughness heights of wind farms. *Renew. Energy* **171**, 34–46.

ZHANG, S., DU, B., GE, M. & ZUO, Y. 2022*a* Study on the operation of small rooftop wind turbines and its effect on the wind environment in blocks. *Renew. Energy* **183**, 708–718.

ZHANG, S., YANG, H., DU, B. & GE, M. 2021*b* Effects of a rooftop wind turbine on the dispersion of air pollutant behind a cube-shaped building. *Theor. Appl. Mech. Lett.* **11** (5), 100296.

ZHANG, Z., HUANG, P., BITSUAMLAK, G. & CAO, S. 2022*b* Large-eddy simulation of wind-turbine wakes over two-dimensional hills. *Phys. Fluids* **34** (6), 065123.

ZONG, H. & PORTÉ-AGEL, F. 2020 A momentum-conserving wake superposition method for wind farm power prediction. *J. Fluid Mech.* **889**, A8.